ENHANCEMENTS TO IMPLICIT SOLVENT MODELING OF PEPTIDES IN WATER AND IN LIPID BILAYERS

by

HUAN ZHAN

A dissertation submitted to the Graduate Faculty in Chemistry in partial fulfillment of the requirements for the degree of Doctor of Philosophy, The City University of New York

2013

© 2013

HUAN ZHAN

All Rights Reserved

This manuscript has been read and accepted for the
Graduate Faculty in Chemistry in satisfaction of the
dissertation requirement for the degree of Doctor of Philosophy.

THEMIS LAZARIDIS

Date | Chair of Examining Committee

MARIA TAMARGO

Date | Executive Officer

THEMIS LAZARIDIS

JOSEPH DANNENBERG

MARCO CERUSO
Supervisory Committee

THE CITY UNIVERSITY OF NEW YORK

ABSTRACT

Enhancements to Implicit Solvent Modeling of Peptides in Water and in Lipid Bilayers

by

Huan Zhan

Advisor: Professor Themis Lazaridis

In recent years implicit solvation models have been increasingly used in molecular dynamics (MD) simulations of proteins/peptides due to their computational efficiency. While these models can account for electrostatic interactions and hydrophobic effect of proteins/peptides in both water and lipid membranes, other properties of the solvent, such as the local dielectric screening effect at the binding sites of metalloproteins, the membrane dipole potential, and the membrane lateral pressure, have not yet been included. In this work, first the effective energy function (EEF1) is extended to simulate metalloproteins by neutralizing ligand carboxylates based on their exposure to solvent water. The new model is then applied to MD simulation of calcium-binding proteins calbindin d9k, calmodulin, troponin C, and parvalbumin. Although structures consistent with experiments are obtained, the model is limited by the fact that the selection of charges for carboxylates is arbitrary, and that the charges cannot be modified as the protein structure changes during the simulation. Second the implicit membrane mode (IMM1) is extended to include the membrane dipole potential, and the new model is applied to MD simulation of the helical peptides alamethicin, WALP23, influenza hemagglutinin fusion peptide, HIV fusion peptide, magainin, and the pre-sequence

of cytochrome c oxidase subunit IV (p25). The results show that the orientation of the peptides in the membrane can be influenced by the dipole potential. In general peptides that tend to insert the N-terminus in the membrane and/or have positively charged side chains will lose binding affinity upon increase of the dipole potential. Finally, IMM1 is extended to include lateral pressure effects and tested by MD simulation of the peptides alamethicin, melittin, cyclotide kalata B1, 18A, and $^{KK}pL_{15}$. The simulations of alamethicin binding to pure DOPC bilayer show that increase in the peptide/lipid molar ratio favors the transmembrane orientation, which is explained by the difference in the cross-sectional area of the two orientations. The simulations of all peptides binding to mixed DOPC/DOPE bilayers show that the binding energy can increase, decrease, or not change as the molar fraction of DOPE increases, which is explained by the difference in the binding location of the peptides.

ACKNOWLEDGMENTS

First, I have to thank my mentor, Dr. Themis Lazaridis, for introducing me to the exciting field of theoretical and computational biophysics. He has given me considerable knowledge, training, supervision and help in a professional way.

I would like to thank Dr. Joseph Dannenberg and Dr. Marco Ceruso for their guidance and helpful discussions. I also thank Dr. M. Mihajlovic, Dr. L. Prieto, Dr. O. Yuzlenko, Dr. A. Manukyan, Dr. A. Rahaman, Dr. A. Brice, Mr. Y. He and other colleagues in the lab for their technical assistance or discussion.

Specially, I have to thank my parents for their tremendous support and endless love to me during my years of education towards a Ph.D. degree. I have to thank my wife for always giving me motivation and support. I thank my best friends for being supportive.

TABLE OF CONTENTS

LIST OF TABLES

LIST OF FIGURES

ABBREVIATIONS

CG	Coarse-grained;
DOPC	1,2-dioleoyl-*sn*-glycero-3-phosphatidylcholine;
DOPE	1,2-dioleoyl-*sn*-glycero-3-phosphatidylethanolamine;
EEF1	Effective energy function 1;
GB	Generalized Born;
GC	Gouy-Chapman;
IMM1	Implicit membrane model 1;
MD	Molecular dynamics;
PB	Poisson-Boltzmann;
RDIE	Distance-dependent dielectric;
RESP	The restrained electrostatic potential;
RMSD	The root-mean-square deviation;

Chapter I

INTRODUCTION

1.1 Molecular dynamics simulation of proteins in solvent

The molecular dynamics (MD) method was first introduced by Alder and Wainwright in the late 1950's to study the interactions of hard spheres (1, 2). In 1964, Rahman carried out the first simulation using a realistic potential for liquid argon (3). In 1974, Rahman and Stillinger did the first MD simulation of a realistic model of liquid water (4). The first protein simulations appeared in 1977 with the simulation of the bovine pancreatic trypsin inhibitor (BPTI) (5). Today MD simulations have been applied to solvated proteins, protein-DNA complexes as well as lipid systems addressing a variety of issues including the thermodynamics of ligand binding and the folding of small proteins. MD simulations of proteins are usually carried out in water or lipid membranes, so the free energy has to include not only the intramolecular energy of the protein (solute), but also the solvation free energy (G^{slv}) arising from the interaction between the protein and surrounding water or lipid molecules (solvent). The traditional way to account for G^{slv} is to first represent the solvent molecules by using atomistic or coarse-grained (CG) model, then calculate the interaction of the solute protein with all these explicitly represented solvent molecules.

1.2 The implicit solvent approach

In an implicit (continuum) solvent model, the solvent is treated as a potential of mean force (PMF). The advantage of doing so is that in order to obtain G^{slv}, we can simply calculate the

interaction of the solute with this potential rather than do the expensive computation with every single solvent molecule. One of the widely used implicit solvent models is the generalized Born (GB) model (6). In the GB model, the polar part of G^{slv} is given by

$$G^{p} = -166\left(1 - \frac{1}{\epsilon}\right)\sum_{i}\sum_{j}\frac{q_i q_j}{\sqrt{r_{ij}^2 + \alpha_i\alpha_j \exp\left(-\frac{r_{ij}^2}{4\alpha_i\alpha_j}\right)}} \tag{1-1}$$

where α is the Born radii and can be obtained by fitting into the solvation energy calculated by the finite difference Poisson-Boltzmann (FDPB) method (7). The non-polar part of G^{slv} is given by

$$G^{np} = \sum_{i}[\gamma(t_i)A_i + \alpha(t_i)] \tag{1-2}$$

where γ and α are adjustable parameters dependent on the atom type t_i, and are both derived from experiments. A_i is the accessible surface area of atom i and is typically calculated by using the "rolling ball" algorithm (8). Finally, the total solvation free energy of in the GB model is given by

$$G^{slv} = G^{p} + G^{np} \tag{1-3}$$

1.3 The effective energy function EEF1

EEF1 (9) is an implicit model for water based on the CHARMM polar hydrogen force field. In EEF1, the "self-energy" due to the interaction between solute and solvent is calculated as

$$\Delta G^{slv} = \sum_{i}\Delta G_i^{slv} = \sum_{i}\Delta G_i^{ref} - \sum_{i}\sum_{j\neq i} f_i(r_{ij})V_j \tag{1-4}$$

where ΔG_i^{ref} is the solvation free energy of atom i, r_{ij} is the distance between i and j, and V_j is the volume of atom j. Eq. 1-4 says that the solvation free energy of atom i is that in a

small model system where the atom is fully exposed to solvent ΔG_i^{ref} minus the solvation free energy it loses due to the presence of surrounding atoms. The solvation free energy density is modeled as a Gaussian function,

$$f_i(r_{ij}) = \frac{\alpha_j}{4\pi r_{ij}^2} \exp\left[-\left(\frac{r_{ij} - R_j}{\lambda_j}\right)^2\right] \quad (1\text{-}5)$$

where R_j is the van der Waals radius of atom j (one half the distance to the energy minimum in the Lennard–Jones potential), λ_j is a correlation length (3.5 Å for most atoms), and α_j is a proportionality coefficient given by

$$\alpha_j = 2\Delta G_j^{free}/\sqrt{\pi}\lambda_j \quad (1\text{-}6)$$

where ΔG_j^{free} is the solvation free energy of the free (isolated) atom j; ΔG_j^{free} is close but not identical to ΔG_j^{ref} and is determined by requiring that the solvation free energy of deeply buried atoms be zero. The above solvation model was added to the CHARMM force field to obtain an approximation for the effective energy of the protein,

$$W_{EEF1} = E + \Delta G^{slv} \quad (1\text{-}7)$$

1.4 The implicit membrane model IMM1

IMM1 (10) is an extension of EEF1 for proteins in membranes. In IMM1, the membrane bilayer is represented by a hydrophobic slab centered at the plane z = 0 Å. The solvation parameters of all atoms (ΔG_i^{ref} and ΔG_i^{free}) now depend on the vertical direction, z, or $z' = |z|/(T/2)$, where T is the thickness of the nonpolar core of the membrane (usually 20 - 30 Å, depending on the lipid),

$$\Delta G_i^{ref}(z') = f(z')\Delta G_i^{ref,wat} + \big(1 - f(z')\big)\Delta G_i^{ref,chex} \quad (1\text{-}8)$$

where $\Delta G_i^{ref,wat}$ is the solvation free energy in water and $\Delta G_i^{ref,chex}$ is the one in cyclohexane. The function $f(z')$ describes the transition from one phase to the other and is defined as

$$f(z') = \frac{z'^n}{1 + z'^n} \tag{1-9}$$

where n controls the steepness of the transition. The exponent n = 10 gives a region of 6 Å over which the environment goes from 90% nonpolar to 90% polar, which corresponds roughly to X-ray and neutron diffraction data for the structure of the lipid bilayers. The midpoint of the transition (f = 0.5) corresponds to the hydrocarbon-polar headgroup interface.

1.5 Electrostatic interactions in EEF1 and IMM1

In EEF1, the electrostatic interactions are treated in two ways: (i) a linear distance-dependent dielectric (RDIE) constant is used (ϵ = r); (ii) the ionic side-chains are neutralized. In IMM1, to account for the strengthening of electrostatic interactions in the membrane in a way that is compatible with RDIE used in EEF1, the dielectric screening function is modified,

$$\epsilon = r^{f_{ij}} \tag{1-10}$$

where f_{ij} depends on the position of the interacting atoms with respect to the membrane and is defined as

$$f_{ij} = a + \left(1 - a\sqrt{f_i f_j}\right) \tag{1-11}$$

In Eq. 1-11, a is an adjustable parameter and is set to 0.85, and f is calculated from Eq. 1-9. Based on Eq. 1-11, far from the membrane, f_{ij} is equal to 1 so that the RDIE model is recovered.

1.6 Electrostatic interactions in anionic lipid membranes

In IMM1, in order to account for the electrostatic interactions between the lipid headgroups and the solute, the venerable Gouy-Chapman (GC) theory for the electrical double layer is adopted (11). In the GC theory, the surface potential, $\psi(0)$, for a symmetric electrolyte is given by

$$\sinh\left[\frac{ze\psi(0)}{2kT}\right] = \frac{\sigma}{\sqrt{8\epsilon_a\epsilon_0 kT\rho}} \tag{1-12}$$

where z is the valence of the electrolyte, e is the charge of a proton, σ is the surface charge density, ϵ_a is the relative permissivity (80 for water), ϵ_0 is the permissivity of vacuum, k is Boltzmann's constant, T is the absolute temperature, and ρ is the number of ions per volume ($\rho = 1000N_{av}c$, where c is the molarity). The potential as a function of distance r outward from the charge surface is

$$\frac{ze\psi(r)}{2kT} = \ln\frac{[1+\alpha\exp(-\kappa r)]}{[1-\alpha\exp(-\kappa r)]} \tag{1-13}$$

where

$$\alpha = \frac{\exp(e\psi(0)/2kT)-1}{\exp(e\psi(0)/2kT)+1} \tag{1-14}$$

And κ is the inverse Debye length, which for a symmetric electrolyte is

$$\kappa = \sqrt{\frac{2\rho Oz^2e^2}{\epsilon_a\epsilon_0 kT}} \tag{1-15}$$

The charge plane is assumed to be at a distance O outward from the nonpolar–polar interface (O is referred to as "offset"). If z = 0 is the midplane of the membrane, T is the thickness of the hydrocarbon region, and O is the offset, then $r = |z| - T/2 - O$. The potential inward from the charge plane (inside the membrane) is constant and equal to the surface potential, that is, $\psi(z) = \psi(0)$ for $|z| < T/2 + O$. No smoothing is done at the boundary.

The electrostatic interaction energy of a peptide in this electrostatic field is given by the sum over all atoms of the product of the electrostatic potential at that point, with the partial charge of the atom, q_i,

$$E_{GC} = \sum_i \psi(z_i) q_i \tag{1-16}$$

1.7 The need for extension of EEF1 and IMM1

In recent years implicit solvation models have increasingly been applied to MD simulation of proteins/peptides due to their computational efficiency. While these implicit solvation models can account for electrostatic interactions and hydrophobic effect of proteins/peptides in both water and lipid membranes, they have the limitations such as the inability to model metalloproteins, the membrane dipole potential, and the membrane lateral pressure. Experiments have shown that these effects could influence the structure as well as activity of proteins/peptides, so their absence in implicit solvation models may cause inaccuracy to MD simulations. Therefore, in this work, we try to establish models to include these effects. The new models are then incorporated in the EEF1 and IMM1 and are applied to the MD simulation of various proteins and peptides.

Chapter II

EXTENDING THE IMPLICIT SOLVENT MODEL EEF1 TO THE MD SIMULATIONS OF METALLOPROTEINS

2.1 Introduction

It is estimated that approximately half of all proteins contain metals (12), and about 30% of all proteins require metals to carry out their function (13). Proteins containing metal ions (metalloproteins) have many important functions including ion storage and transport, catalysis, and signal-transduction.

Among metalloproteins, the calcium-binding proteins, such as calbindin d9k, calmodulin, troponin C, and parvalbumin, are responsible for signal-transduction within cells. The binding (active) sites of the calcium-binding proteins are found to be highly conserved and are called EF-loops (14). An EF-loop consists of 12 residues, among which the first, third, fifth, seventh, ninth, and twelfth residues are usually labeled as X, Y, Z, -Y, -X, and –Z. The –Z residue is invariably a glutamate, and the –Y residue is sometimes replaced by a water molecule from solvent. Experiments show that except the –Z glutamate that binds with both carboxylate oxygens, each residue contributes only one oxygen for binding, either from backbone or side chains. EF-loops are highly selective in binding Ca^{2+}, whose binding equilibrium constant is about 4000 times larger than that of Mg^{2+} despite the similarity in both size and charge between the two ions (15).

MD simulations with explicit water models such as SPC, TIP3P, and TIP4P have been widely used to study the structure of metalloproteins (16-25). Compared with *ab initio*

computations, MD simulations have the advantage of being applicable to large systems. However, since the force field parameters depend on the nature of metal ion and its ligands, they must be calculated and tested on each individual system before being used in MD simulations (26).

In recent years implicit solvation models have also been applied to MD simulation of proteins/peptides in water and membranes due to their computational efficiency (10, 27-30). Although metal ions have proven crucial for both structure and activity of metalloproteins, they have not yet been incorporated into implicit solvation models. So the objective of this study is to extend the implicit solvation model to the MD simulation of metalloproteins, and thereby enable us to investigate the thermodynamics of the binding process of metal ions, and reproduce the experimental binding selectivity between metal ions.

In this study, we extended the implicit solvation model EEF1 (27) to MD simulation of calcium-binding proteins in water. Since the interaction between Ca^{2+} and ligands is mainly electrostatic, it is influenced by both charge transfer between Ca^{2+} and ligands, and dielectric screening effect of solvent water. In order to investigate the influence of charge transfer, the EEF1 charges are replaced by the charges from *ab initio* computation at the binding sites of parvalbumin. The new charge set is then applied to the MD simulation of parvalbumin, and the resulting structure is compared with the crystal structure. In order to investigate the influence of local dielectric screening effect of solvent water, instead of being neutralized completely as in EEF1, the ligand carboxylates at the binding sites are neutralized differently based on their exposure to water in the crystal structures. The resulting charge set is then applied to the MD simulation of calbindin d9k, calmodulin, troponin C, and parvalbumin.

2.2 Methods

2.2.1 The parameterization of Ca^{2+}

The van der Waals parameters of Ca^{2+} were taken from the study of Marchand and Roux (ε = -0.12 kcal/mol, σ = 2.435717 Å) (18). The solvation free energy parameters (ΔG^{ref} and ΔG^{free}) were taken from the experimental hydration free energy of Ca^{2+} (-381 kcal/mol) (31), but the value was arbitrarily scaled down to -30 kcal/mol to prevent Ca^{2+} from moving away from the binding site during MD simulations. The charge of Ca^{2+} was set to +2, which was replaced by the value from *ab initio* computation in the study of charge transfer.

2.2.2 The *ab initio* computation of charges at the binding sites

The *ab initio* computation of charges at the binding sites of parvalbumin was carried out with the Gaussian98 program (32). First the binding sites of parvalbumin (the seven residues coordinating Ca^{2+} in each EF-loop) were extracted from the crystal structure (PDB entry: 2PVB) and were optimized by using the semi-empirical PM3 (parameterized model 3) method. Then atomic charges were calculated by using the HF (Hartree Fock) method with the 6-31G* basis set.

2.2.3 The MD simulations

MD simulations were carried out with the CHARMM program (33). The proteins were simulated in water by using the implicit solvation model EEF1. Each simulation lasted 1 ns. The crystal structures of calbindin d9k (3ICB), calmodulin (1CDM), troponin C (5TNC), and parvalbumin (2PVB) were used as the initial structures for the MD simulations.

2.3 Results and discussion

2.3.1 Charge transfer between Ca^{2+} and ligands

In order to investigate the influence of charge transfer on the binding structure of parvalbumin, MD simulations were performed with three different charge sets: (i) the EEF1 charge set (C_{EEF1}), in which the ionic side chains are neutralized; (ii) the EEF1 charge set with charges at the binding sites replaced with the standard CHARMM charges (C_{CHARMM}), in which the ionic side chains are charged; (iii) the EEF1 charge set with the charges at the binding sites re-calculated by *ab initio* method (C_{AB}), in which the ionic side chains are charged. Of all three charge sets, only the third one takes the charge transfer between Ca^{2+} and ligands into consideration. Since it was found that the –Y water molecule easily moves away from the binding sites during the simulation, harmonic constraint was placed on the position of the water molecule. The distances between Ca^{2+} and binding oxygens (d(Ca-O)) from the simulations are summarized in Table 2.1 and are compared with those measured from the crystal structure. It can be seen from the table that d(Ca-O) in the crystal structure is around 2.2-2.4 Å, which is in general a little larger than the values calculated with all three charge sets. For the second carboxylate oxygen of the –Z glutamate at both binding sites of parvalbumin, simulation with C_{EEF1} gives a d(Ca-O) around 3.5 Å, which is much larger than the experimental value. For the same oxygen, simulation with C_{AB} gives a d(Ca-O) around 3.0 Å, which is inconsistent with experiment either. The reason for this could be that beside electrostatic interaction, there also exists bond interaction between Ca^{2+} and ligands, which is not considered in our model.

TABLE 2.1 Distance (Å) between Ca^{2+} and binding oxygens in parvalbumin. The distance is calculated from the minimized structures. * Distance in the crystal structure (2PVB).

	Ligand	C_{EEF1}	C_{AB}	C_{CHARMM}	Exp*
	D52/OD1	2.29	2.28	2.17	2.23
	D54/OD1	2.36	2.25	2.16	2.35
Loop1	S56/OG	2.09	2.19	2.22	2.59
	F58/O	2.16	2.27	2.28	2.26
	E60/OE1	2.27	2.26	2.18	2.48
	E63/OE1	3.55	3.06	2.51	2.55
	E63/OE2	2.31	2.33	2.23	2.43
	D91/OD1	2.27	2.38	2.20	2.24
	D93/OD1	2.40	2.27	2.23	2.41
	D95/OD1	2.25	2.30	2.21	2.43
Loop2	K97/O	2.11	2.19	2.26	2.29
	E102/OE1	2.30	2.33	2.20	2.50
	E102/OE2	3.44	2.99	2.76	2.48
	H_2O/O	2.01	2.19	2.07	2.51

2.3.2 Local dielectric screening effect at the binding sites

The electrostatic interaction between Ca^{2+} and ligands is influenced by the dielectric screening effect of water. The dielectric constant ε is around 80 in bulk water, and about 2-4 inside proteins (34). In EEF1, to account for this effect, first a linear distance-dependent dielectric constant (ε = r) is used, and ionic side chains are neutralized. In this study, we modified this neutralization for the carboxylates of ligand aspartates and glutamates at the binding sites. The carboxylates of aspartates and glutamates are now neutralized based on their exposure to solvent water. In the MD simulation, the constraint on –Y water in the

previous simulation was removed. Each simulation was repeated ten times and the percentage of obtaining binding structures consistent with the crystal structure was calculated. The result was then compared with the simulations with C_{EEF1} and C_{CHARMM}.

2.3.3 MD Simulations with C_{EEF1} and C_{CHARMM}

The charges on carboxylates in C_{EEF1} and C_{CHARMM} are shown in Figure 2.1. With C_{EEF1} and C_{CHARMM}, MD simulations were run on calbindin d9k, calmodulin, troponin C, and parvalbumin. The result of the simulation is summarized In Table 2.3. It can be seen from the table that in all simulations with C_{EEF1}, no structure consistent with the crystal structures was obtained. In the simulation with C_{CHARMM}, the average percentage of finding structures consistent with the crystal structures is 45%.

FIGURE 2.1 Charges of carboxylates in C_{EEF1} (left) and C_{CHARMM} (right)

2.3.4 MD Simulations with charges based on the exposure to solvent water

The exposure coefficient of atom i is defined based on the solvation free energy density in EEF1 (27),

$$EX_i = \sum_{j \neq i} f_i(r_{ij}) V_j \qquad (2\text{-}1)$$

in which $f_i(r_{ij})$ and V_j are defined in (1-5). Based on Eq. 2-1, if an atom is less exposed to

water, it will be surrounded by more protein atoms and EX will be larger; on the other hand, if an atom is more exposed to water, it will be surrounded by less protein atoms and EX will be smaller. By using Eq. 2-1, EX of carboxylates (ligand aspartates and glutamates) at the binding sites was calculated. Since the dielectric screening to an atom is caused by the dipoles of surrounding water molecules and is affected by the number of water molecules, it is reasonable to make the assumption that the intensity of the screening is related to EX. Therefore, based on EX, we divided the carboxylates into three groups: carboxylates in the first group have an EX below 2.0, and are considered to be the most exposed; carboxylates in the second group have an EX between 2.0 and 2.2, and are considered to be medium exposed; carboxylates in the third group have an EX over 2.2, and are considered to be the least exposed. Then, charges of carboxylates in the three groups are modified in order to reflect the difference in dielectric screening intensity caused by EX (Table 2.2). This new charge set is labeled as C_{EX}.

TABLE 2.2 The exposure coefficient EX and corresponding charges of carboxylates. Only the charge of the carbon atom is adjusted.

Protein	Residue	EX	Charge
1CDM	D55	1.48	
1CDM	D48	1.49	
2PVB	D91	1.53	
1CDM	D12	1.54	
2PVB	D93	1.71	Most exposed
2PVB	D52	1.73	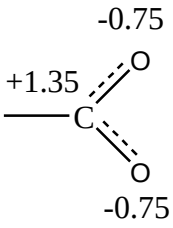
1CDM	D21	1.75	
1CDM	D19	1.79	
1CDM	D50	1.79	
5TNC	D19	1.83	
3ICB	D58	1.91	
5TNC	D55	1.91	
1CDM	D46	1.97	
1CDM	D17	2.01	
2PVB	D89	2.03	Medium exposed
5TNC	D51	2.05	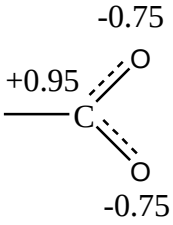
1CDM	D53	2.10	
2PVB	E58	2.13	
1CDM	D10	2.15	
5TNC	D15	2.18	

TABLE 2.2 (Continued)

Protein	Residue	EX	Charge
2PVB	E100	2.26	
1CDM	E57	2.32	
3ICB	D54	2.32	
5TNC	E26	2.35	Least exposed
1CDM	E28	2.36	
1CDM	E64	2.40	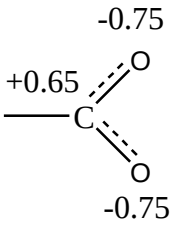
2PVB	D50	2.42	
1CDM	E21	2.50	
5TNC	E63	2.50	
2PVB	E61	2.53	
3ICB	E65	2.84	

With C_{EX}, MD simulations were run on calbindin d9k, calmodulin, troponin C, and parvalbumin again. The result is also given in Table 2.3. It can be seen from the table that the average percentage of finding structures consistent with the crystal structures increases to 83%, which is much better than the simulations with C_{EEF1} and C_{CHARMM}. Although C_{EX} gives better result than C_{EEF1} and C_{CHARMM}, it has to be pointed out that the selection of the charges for carboxylates in C_{EX} is totally arbitrary. Also, C_{EX} has to be determined before the MD simulation based on the crystal structures of proteins, and cannot be changed during the simulation even if the conformation of the protein changes.

TABLE 2.3 Results of MD simulations with C_{EEF1}, C_{CHARMM}, and C_{EX}.

	1CDM				2PVB		3ICB		5TNC		p%
	EF1	EF2	EF3	EF4	EF1	EF2	EF1	EF2	EF1	EF2	
C_{EEF1}	0	0	0	0	0	0	0	0	0	0	0%
C_{CHARM}	8	4	8	3	4	3	5	4	4	0	45%
C_{EX}	8	7	10	9	8	9	9	10	8	9	88%

The number in each column is the structures from simulation (out of a total of 10) having the same coordination number as the crystal structures. The average percentage (p%) is given in the last column.

2.4 Conclusion

In this study, we tried to extend the implicit solvation model EEF1 to the MD simulation of calcium-binding proteins. The interaction between Ca^{2+} and its ligands is considered to be mainly electrostatic and influenced by both charge transfer between Ca^{2+} and ligands, and the dielectric screening effect of solvent water. In order to investigate the influence of charge transfer on the binding structure, the charges at the binding sites of parvalbumin were re-calculated by using *ab initio* method and then used in the MD simulation of parvalbumin. The result shows that the binding structure is inconsistent with the crystal structure in that the –Z glutamate of the EF-loops binds with only one carboxylate oxygen. The reason for this could be that there is bond interaction between Ca^{2+} and ligands, which is not included in our model.

In the study of local dielectric screening effect at the binding sites, for carboxylates of ligand aspartates and glutamates, the exposure coefficient to water is calculated based on the crystal structures of the proteins. Then the carboxylates are neutralized differently based on their exposure coefficients. The new charge set was then used in the MD simulation of

calbindin d9k, calmodulin, troponin C, and parvalbumin. The result shows that the binding structure is more consistent with the experiment compared with C_{EEF1} and C_{CHARMM}. The limitation of this method is: (i) the selection of charges for carboxylates in each group is arbitrary; (ii) the exposure coefficient has to be calculated before the MD simulation and cannot be modified during the simulation.

Chapter III

INFLUENCE OF THE MEMBRANE DIPOLE POTENTIAL ON PEPTIDE BINDING TO LIPID BILAYERS

3.1 Introduction

There are three electrostatic potentials associated with cellular lipid bilayers (35, 36). The transmembrane potential $\Delta\psi$ is caused by the difference in charge concentration in the two bulk phases across the membrane; the surface potential ψ_s arises from the presence of net charge at the membrane surface; and the dipole potential ψ_d is thought to arise from the alignment of lipid and water molecule dipoles. The dipole potential ψ_d was discovered in studies of ion-transport across membranes (37-39) and has attracted great interest since it can significantly influence many important physiological processes such as ion permeability, voltage-gated channels, and function of membrane proteins. The dipole potential is commonly attributed to two factors: a negative contribution from lipid polar groups (the P-N dipole of phosphatidylcholine and the C-O dipole of carbonyl), and a positive contribution from interfacial water molecules (40). The former is apparently over-compensated by the latter, leading to a positive total potential in the lipid hydrophobic core (41-50). It should be noted that, despite its name, ψ_d could contain significant quadrupolar contributions, as was clearly shown for liquid-vapor interfaces (51-53).

Several techniques have been developed to measure ψ_d in experiments, including ion permeability (54), electron paramagnetic resonance (55), lipid monolayers (56), voltage-sensitive dye fluorescence (57), and cryo-EM (58). Although it is agreed that the

potential is positive in the lipid hydrophobic core, its magnitude varies depending on the technique used (39, 41, 55, 56, 58-61). From potential measurements across a PC monolayer at the air-water interface, values of 390-440 mV were obtained (39, 59), whereas from the differential membrane conductance induced by organic cations, values of 197-240 mV were obtained (41, 55, 59). The membrane dipole potential could also be influenced by lipid composition. For example, it was found that the potential of a DMPC monolayer is 449.1 mV, while that of an anionic DMPG is 301.8 mV (62), and the potential of a pure DMPC vesicle is 410 mV, while the value for a hybrid DMPC/MMPC vesicle is 268 mV (63).

Another way to modify the membrane dipole potential is to add specific compounds to the solution (64-67). Among these compounds, 6-ketocholestanol (6-KC) increases ψ_d, while phloretin or phlorizin decrease it. Cholesterol also raises ψ_d but less effectively than 6-KC. The reason that ψ_d is affected by these compounds could be the dipole of these molecules, or that they can change the packing of the headgroups and/or the orientation of interfacial water molecules (68).

The dipole potential might influence the structure and function of membrane-active peptides. In one study it was found that phlorizin modulated alamethicin activity, possibly by affecting its tilt angle or depth of insertion in the membrane (69). The influence of ψ_d on peptide orientation could be crucial in physiological processes like membrane fusion, which is facilitated by so called fusion peptides. These peptides are presumed to adopt specific angles with respect to the membrane (70), which may be manipulated by the membrane dipole potential.

Molecular dynamics (MD) simulations with explicit solvent have been extensively used

to investigate ψ_d in lipid membranes (42-50, 52, 53, 71-77). The dipole potential is calculated as a double integral of charge density along the membrane normal. All simulations give a positive potential in the membrane interior relative to water. As to the magnitude of ψ_d, however, the simulations are not consistent. With the GROMOS force field and SPC water, Tieleman and Berendsen obtained a value of 250 mV for a DPPC bilayer (45). The potential was as high as 1000 mV in another simulation with the AMBER force field and TIP4P water (46). A third study that used the AMBER force field but charges from ab initio calculation, gave a value of 960 mV (47). With similar parameterization, Smondyrev and Berkowitz found that ψ_d ranges between 600 mV and 1000 mV for a hybrid DPPC/cholesterol bilayer (50). Besides the force field, truncation of electrostatic interactions (75) and polarization (53, 73) also have profound influence on the calculated potential. It is worth pointing out that the potential obtained from simulations is a theoretical idealization that cannot be experimentally measured, since any experiment would have to use a finite-size probe that would inevitably perturb the membrane (78).

In recent years implicit solvation models have also been applied to MD simulation of peptides in membranes due to their computational efficiency (10, 28-30). Although the membrane dipole potential has been proven crucial for lipid membranes and their interaction with peptides, it has not yet been incorporated into implicit membrane models. This could cause inaccuracies due to the omission of electrostatic interaction between the potential and the peptide dipole. In this study, we implement the membrane dipole potential into the IMM1 implicit membrane model (10). With the new model, we investigate the interaction between a zwitterionic bilayer and the helical peptides alamethicin, WALP23, influenza hemagluttin

fusion peptide (HAFP), HIV fusion peptide (HIVFP), magainin, and the pre-sequence of cytochrome c oxidase subunit IV (p25). The influence of the membrane dipole potential on peptide orientation and binding energy are determined and discussed.

3.2 Methods

3.2.1 The membrane dipole potential model

Explicit MD simulations give a positive potential in the membrane interior relative to water. Its magnitude varies depending on lipid type and simulation force field (42-50, 52, 53, 71-77). The width of the transition region (the region over which the change between high potential in the membrane interior and low potential in water takes place) seems to be around 10 Å, while the position varies slightly depending on lipid composition. In many simulations the potential profile is monotonic (42-47, 52, 53, 68, 71-74) but in others a small peak was found on the membrane side of the transition region (45, 48-50, 75-77). This could be caused by local changes at the interface due to surface tension, as discussed by Tieleman and Berendsen (45). In their simulation of a DPPC bilayer, similar peaks were found in the NVT and NγT systems but not in the NPT system. Given the disagreement in simulation results and to keep the model simple, we decided to use a monotonic potential profile.

The following function was chosen to mimic the membrane dipole potential:

$$\psi_d = \frac{c}{1 + a|z|^b} \quad , \tag{3-1}$$

where a, b, and c are parameters and z is the distance to the bilayer center. The position and the width of the transition region are controlled by parameters a and b, which are set to 6.23×10^{-7} and 5.5, respectively. This places the center of the region around 13.5 Å,

corresponding to the hydrophobic boundary of the POPC bilayer. This choice of parameters gives an approximate 10 Å for the width of the transition region. While the shape of the potential curve is controlled by a and b, the height is only determined by c. Unlike a and b that are fixed throughout the simulations, c is varied

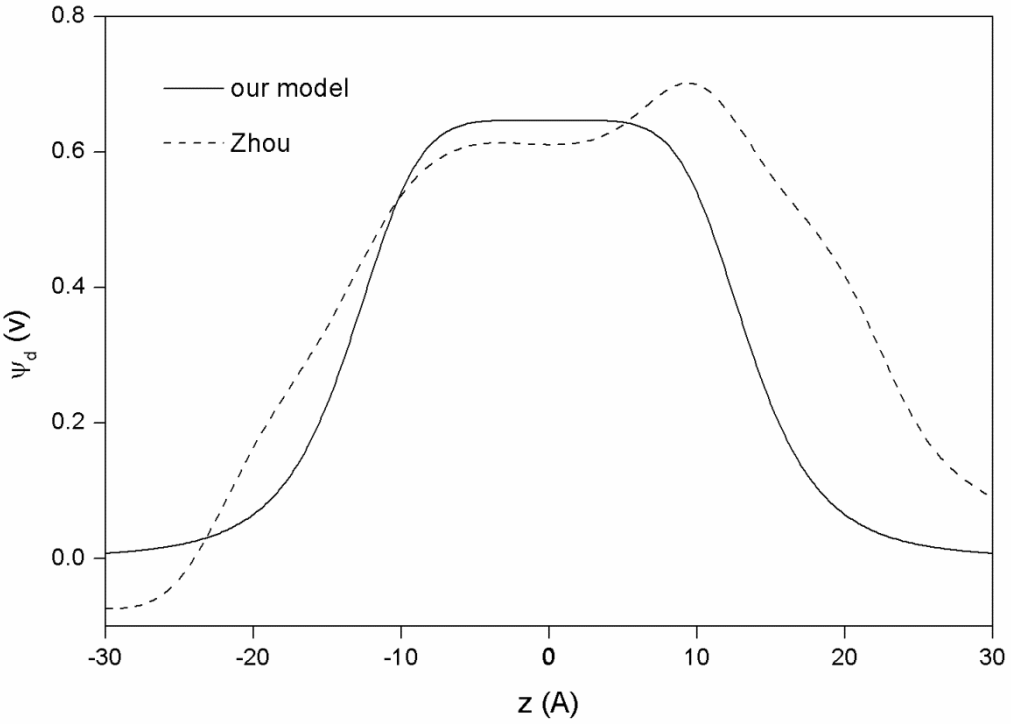

FIGURE 3.1 Dipole potential profiles across a bilayer from the explicit MD simulation of Zhou and Schulten (44) (dashed line) and from our model (solid line). In our model, the potential is symmetric with respect to the bilayer center, as it should for a symmetric bilayer.

from 0 mV to 400 mV. In this way, the interaction between the membrane bilayer and peptides at various ψ_d could be investigated. Figure 3.1 compares the potential profile from our model (Eq. 3-1) to that from the explicit MD simulation by Zhou and Schulten (44). It can be seen that there is good correspondence between them. In this implementation the dipole potential profile, like standard IMM1, is symmetric with respect to the bilayer center.

It thus describes symmetric bilayers, like those for which the potential profile has been calculated by explicit simulations. More realistic cell membranes with different intracellular and extracellular leaflet compositions could be treated in the future by a straightforward extension of the model.

The energy of interaction of a solute with the membrane dipole potential is implemented as an extra term in IMM1:

$$\Delta G^{dp} = \sum_i q_i \psi_d \quad , \tag{3-2}$$

where q_i is the charge of atom i. As was done in the treatment of the surface potential (11), ionic side-chains carry a full charge in the calculation of the dipole potential energy term but are neutral in the calculation of intra- or inter-peptide interactions, as EEF1 and IMM1 require.

3.2.2 Molecular dynamics simulations

MD simulations were carried out with the CHARMM program (33). Membrane and water were implicitly represented with IMM1. Six peptides were simulated: alamethicin, WALP23, HAFP, HIVFP, magainin, and p25. Their sequences are shown in Table 3.1. All peptides were simulated in a zwitterionic (neutral) bilayer except p25, for which an anionic bilayer was used with 30% anionic lipids. This choice was made because it has been reported that little or no helical structure was detected for p25 in membranes containing less than 20% negatively charged lipids (79). The initial helical structures of the peptides were generated by CHARMM based on their sequences. At the beginning of the simulations, HAFP, HIVFP, magainin, and p25 were placed parallel to the membrane plane with their hydrophobic face

TABLE 3.1 Simulated peptides and their sequences. U in alamethicin represents 2-aminoisobutyric acid. Charged residues are underscored.

alamethicin	Ac-UPUAUAQUVUGLUPVUUEQF-OH
HAFP	Ac-GLFGAIAGFIENGWEGMIDG-CONH2
HIVFP	Ac-AVGIGALFLGFLGAAGSTMGARS-CONH2
magainin	Ac-GIGKFLHSAKKFGKAFVGEIMNS-CONH2
p25	Ac-MLSLRQSIRFFKPATRTLCSSRYLL-CONH2
WALP23	Ac-GWWLALALALALALALALALWWA -CONH2

toward the membrane. For alamethicin, both interfacial orientation (alamI) and transmembrane orientation (alamT) were simulated, and for WALP23 only the transmembrane orientation was considered. All helices were first simulated for 5 ns without the dipole potential. For interfacial orientations, besides the placement with the hydrophobic face toward the membrane, the helices were also rotated by various angles around their long axes and simulated for 25 ns. The simulations gave similar equilibrated structures for all initial orientations, showing that the results are not significantly influenced by the initial conditions. After the simulation without the dipole potential, another 5 ns simulation was run on the final structures at five different ψ_d values (0 mV, 100 mV, 200 mV, 300 mV, and 400 mV). Each simulation was repeated eight times with different initial velocities, based on which the standard deviation of tilt angle and binding energy were calculated. For comparison, an extended 25 ns simulation was also performed on each peptide at 200 mV, and the energy, the tilt angle, and the RMSD over the trajectory were calculated. The results (not shown in the paper) show that the energy converges rapidly during the simulations. The tilt angle and RMSD also converge within the first 2 ns of the simulations for all the peptides

except HIVFP and p25. The tilt angle and RMSD of HIVFP and p25 exhibit larger fluctuations than in the other peptides because, as can be observed during the simulation, the termini of the two peptides tend to unfold. Average structures and energies of the last 2 ns were taken for analysis. The binding energy of the peptides was estimated as the average effective energy difference in membrane and water environments for the conformational ensemble generated by the membrane simulation:

$$E_{binding} = \frac{1}{N}\sum_{i=1}^{N}\left(E_i^{mbr} - E_i^{wat}\right) \quad , \tag{3-3}$$

where E_i^{mbr} and E_i^{wat} are the effective energy in membrane and in water respectively. The index i runs through N = 1000 conformations saved at equal intervals within the last 2 ns of the simulation. Qualitatively similar results were obtained by averaging the effective energy in independent simulations in water and membrane and taking the difference. In that approach the statistical uncertainties were significantly larger.

3.3 Results

3.3.1 Influence of the membrane dipole potential on peptide orientation

The starting configuration of all helices was parallel to the membrane plane except for alamT and WALP23, for which it was perpendicular to the membrane plane. During the course of the simulation they adopted the tilt angles (θ) shown in Table 3.2. Figures 3.2-3.5 show their average orientations at different values of the dipole potential. Magainin remains almost perfectly parallel to the membrane. HAFP adopts a slight tilt. Increasingly larger tilts (smaller tilt angles) are adopted by alamI, HIVFP, and p25. WALP23 (not shown) adopts an almost

TABLE 3.2 Tilt angles of the helices on membrane bilayer

ψ_d (mV)	0	100	200	300	400
alamI	69.5 (±0.9)	71.4 (±1.4)	84.9 (±0.7)	86.9 (±0.1)	88.8 (±0.2)
alamT	28.8 (±1.1)	26.0 (±1.2)	22.5 (±0.9)	18.5 (±0.5)	16.6 (±0.5)
HAFP	80.0 (±2.1)	82.6 (±1.1)	83.0 (±1.6)	84.3 (±1.6)	86.0 (±0.7)
HIVFP	33.0 (±6.5)	31.3 (±8.5)	36.5 (±1.2)	36.5 (±2.3)	37.3 (±2.1)
magainin	86.6 (±0.2)	88.0 (±0.9)	89.2 (±1.8)	90.5 (±1.9)	95.5 (±5.0)
p25	61.5 (±4.5)	60.8 (±3.4)	62.9 (±7.1)	66.6 (±3.5)	65.4 (±5.2)
WALP23	10.3 (±0.7)	10.5 (±0.4)	10.8 (±0.7)	11.2 (±0.7)	11.4 (±0.7)

The tilt angle (in degrees) is calculated as the angle between helix axis and membrane normal. Standard deviation is given in parenthesis. AlamI refers to the interfacial orientation, and alamT refers to the transmembrane orientation.

perpendicular orientation to the membrane and its tilt angle is insensitive to the dipole potential. AlamT is more tilted and its tilt angle decreases with the dipole potential.

Figure 3.2 shows the orientation of alamethicin at various values of ψ_d. For alamI, it can be seen that when ψ_d is set to 0 mV, the helix has an average $\theta = 69.5^o$. As ψ_d increases, the N-terminus gradually moves out of the membrane while the C-terminus remains at the same position. This result is consistent with the proposal of Luchian and Mereuta on the effect of phlorizin on alamethicin orientation (69). Another interesting observation is that the relation between ψ_d and helix re-orientation is not linear. Re-orientation happens faster at low potential (between 0 mV and 200 mV), and slows down beyond that.

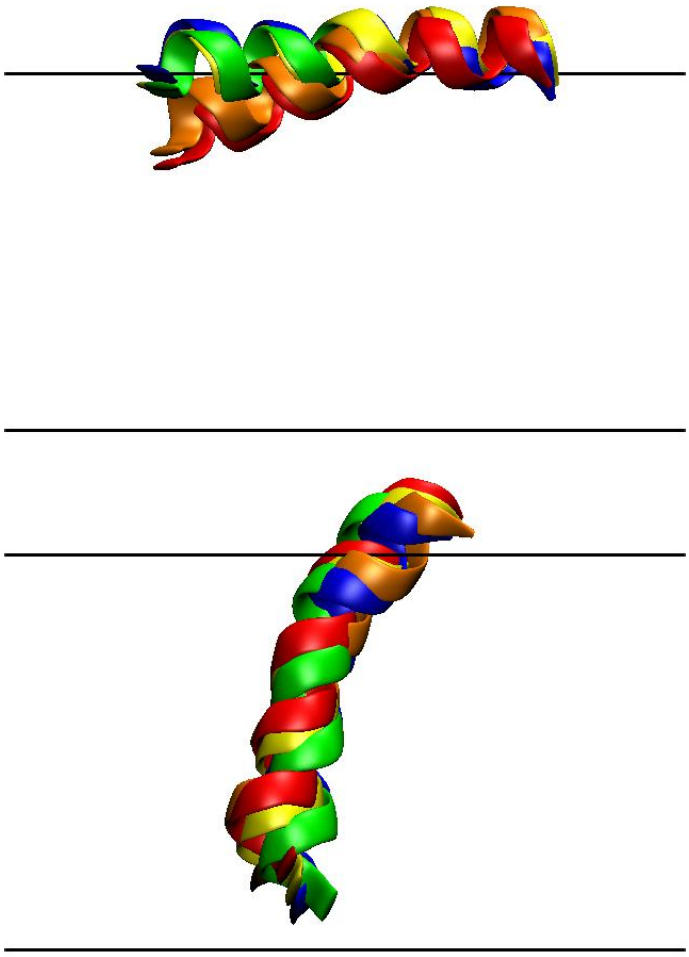

FIGURE 3.2 Orientations of alamI (top) and alamT (bottom). Orientations at various ψ_d are labeled as: red, 0 mV; orange, 100 mV; yellow, 200 mV; green, 300 mV; blue, 400 mV. Black lines denote the bilayer boundary. The N-terminus is toward the left for alamI and toward the bottom for alamT.

For alamT, the simulation gives an average $\theta = 28.8^o$ at 0 mV, a little larger than the 17^o obtained by Bak et al. in their solid-state NMR experiment (80). As ψ_d increases to 400 mV, the tilt angle of alamT decreases to 16.6^o. The tilt angle of the other transmembrane helix WALP23 is around 10.0^o, smaller than the value around 30^o given by previous experimental and explicit simulation studies (81-83). The reason for this is probably that in those studies thinner bilayers were used, such as DMPC. Unlike alamT, there is no significant change in the angle for WALP23 from 0 mV to 400 mV.

In Figure 3.3 the orientations of HAFP and magainin are shown. Unlike alamI, the N-termini of HAFP and magainin stay much closer to the membrane surface. The tilt angles of the two helices are close to each other at ψ_d = 0 mV, and the values of 80.0^o and 86.6^o are in good agreement with the 77.6^o and 80^o, respectively, obtained in previous studies (84, 85). The tilt angles of both helices increase slightly with the dipole potential to a final value around 86.0^o and 95.5 ^{o} at 400 mV.

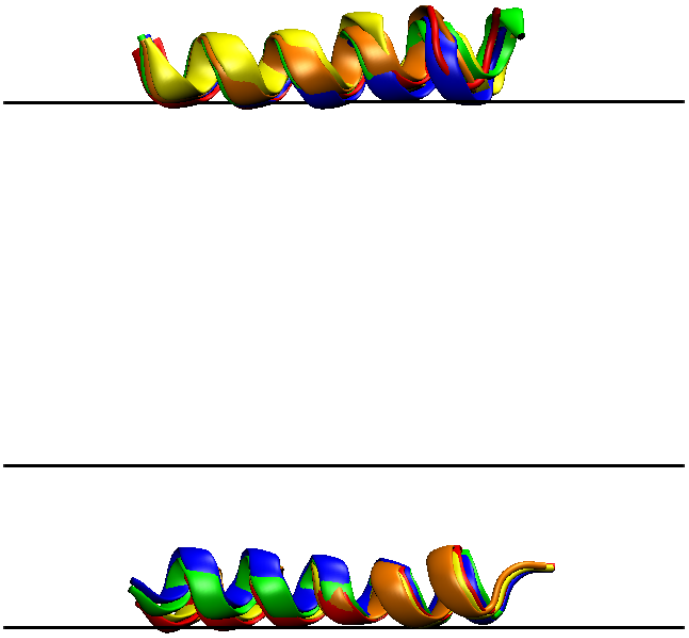

FIGURE 3.3 Orientations of HAFP (top) and magainin (bottom). The N-terminus is toward the left for both HAFP and magainin. The color labeling is the same as in Figure 3.2.

HIVFP (Figure 3.4) at ψ_d = 0 mV adopts a large tilt angle, θ = 33.0^o, and a very deep insertion of the (acetylated) N-terminus that almost reaches the bilayer center. The tilt angle is

in good agreement with the 36.5° in DOPC/Chol/DOPE/DOPG multilayer and the 39.0° in DMPC bilayer obtained spectroscopically (86), and a little smaller than the 44.0° obtained in an explicit MD simulation (87). The angle increases slightly with dipole potential to 37.3°. Relatively large error bars are observed for this peptide, probably because, as we observed from the simulation trajectory, the helix C-terminus is unstable and easily unfolds.

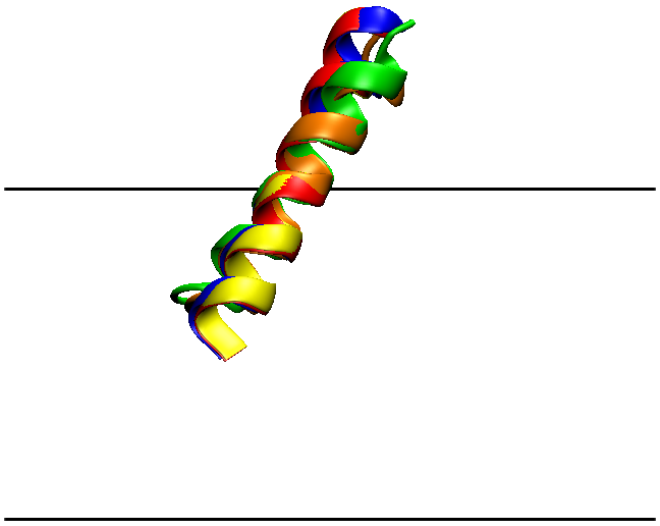

FIGURE 3.4 Orientation of HIVFP. The N-terminus is toward the left. The color labeling is the same as in Figure 3.2.

The behavior of p25 is a little different from that of the other helices (Figure 3.5). From 0 mV to 400 mV the tilt angle increases slightly. However, it can be seen from the figure that as ψ_d increases, there is a clear shift along the membrane normal for the whole helix. This is probably due to the five cationic side-chains, which are evenly distributed along the helix axis. As the membrane dipole potential increases, the interaction between the potential and the cationic side-chains pushes both termini away from the bilayer. It was found that the helical structure of p25 is very unstable and easily unfolds, probably because p25 is located in

a more aqueous environment than the other helices. This is consistent to what one would expect from simple arguments based on hydrophobicity and electrostatics (88), although some experimental results seem to suggest that the helices are inserted into the lipid membrane parallel to the lipid acyl chains (89).

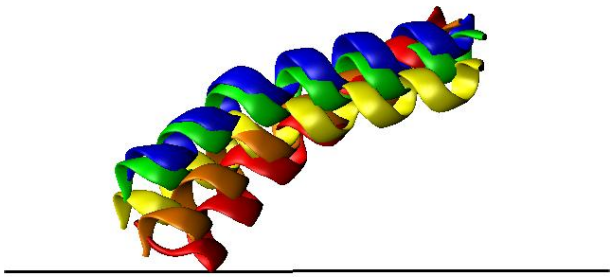

FIGURE 3.5 Orientation of p25. The N-terminus is toward the left. The color labeling is the same as in Figure 3.2.

To explain the re-orientation that takes place for some peptides one has to consider the interaction with the membrane dipole potential of two factors: the backbone dipole and ionic side-chains. It is well known that in a helix the aggregate effect of all the individual dipoles from the CO and NH groups creates an overall dipole moment that points from its N-terminus to C-terminus. When placed in an external electric field, which in this study is the membrane dipole potential induced by lipid headgroups and interfacial water molecules, the dipole of the helix will adjust its orientation to achieve optimal alignment to the field. Since the potential is more positive in the lipid hydrophobic core than in water, the N-terminus tends to

be expelled from the membrane interior while the C-terminus is attracted to the membrane. Ionic side-chains could have considerable electrostatic interaction with the dipole potential, although their favorable solvation in water forces them to avoid the membrane interior where the dipole potential is stronger. Still, cationic side-chains should be pushed away from the membrane and anionic side-chains should be attracted to the membrane.

The effect of the backbone dipole is most clearly demonstrated in the case of alamI, which shows a large increase in tilt angle as the dipole potential increases from 0 mV to 400 mV. An increase is also observed for HIVFP but it is much smaller. One possible reason for this difference in behavior between alamI and HIVFP is that on the C-terminal side alamI has an anionic glutamate, while HIVFP has a cationic arginine. These will also interact with the membrane dipole and either act in concert (as in alamI) or oppose (as in magainin) the reorientation induced by the backbone dipole. Another possibility is that the backbone dipole interaction with the membrane dipole is not strong enough in the case of HIVFP to overcome the natural tendency of this peptide for oblique orientations that results from a hydrophobicity gradient along its helical axis (70).

Transmembrane helices such as WALP23 show smaller interactions with the dipole potential because their interactions with each leaflet partly cancel out. AlamT does not completely cross the bilayer and has its N terminus on the opposite leaflet. It can, therefore, interact more strongly with the dipole potential. Its tilt angle decreases and its N-terminus moves towards the opposite interface as the dipole potential is increased. This shift improves favorable interactions of the N-terminus with the dipole potential on the trans side of the bilayer.

3.3.2 Influence of the membrane dipole potential on binding energy

The membrane binding energy (ΔG^o) of the peptides is estimated as the average effective energy change upon moving the peptides from water into the bilayer. The results are summarized in Table 3. For alamI, magainin, and p25, ΔG^o increases (binding affinity decreases) by 1.4-3.7 kcal/mol from 0 mV to 400 mV. For transmembrane helices alamT and WALP23, ΔG^o increases by smaller amounts, 1.0 kcal/mol and 0.9 kcal/mol from 0 mV to 400 mV. Among all helices, HIVFP has the largest ΔG^o increase of 5.1 kcal/mol. HAFP is the only peptide that gains membrane affinity as the dipole potential increases.

The loss of membrane binding affinity as the dipole potential increases for alamI and HIVFP can be explained by the interaction between the potential and the helix backbone dipole. Both of these peptides insert their N-termini into the membrane. Since the helix backbone dipole is from N-terminus to C-terminus, and the membrane dipole potential is higher inside the membrane, the electrostatic interaction between the potential and the dipole is unfavorable and becomes more unfavorable as ψ_d increases.

TABLE 3.3 Relative binding energy of the peptides to the membrane

ψ_d (mV)	0	100	200	300	400
alamI	0.0 (±0.2)	1.0 (±0.2)	1.4 (±0.1)	1.5 (±0.1)	1.4 (±0.1)
alamT	0.0 (±0.2)	0.4 (±0.2)	0.7 (±0.2)	1.1 (±0.1)	1.0 (±0.2)
HAFP	0.0 (±0.6)	-0.9 (±0.8)	-0.4 (±0.2)	-1.2 (±0.9)	-3.1 (±0.8)
HIVFP	0.0 (±0.6)	1.5 (±0.7)	2.4 (±0.4)	3.6 (±0.2)	5.1 (±0.4)
magainin	0.0 (±0.2)	0.9 (±0.4)	1.5 (±0.5)	2.0 (±0.4)	2.6 (±0.5)
p25	0.0 (±0.8)	1.1 (±1.0)	2.1 (±0.7)	3.4 (±0.1)	3.7 (±0.4)
WALP23	0.0 (±0.5)	0.1 (±0.5)	0.7 (±0.5)	0.7 (±0.5)	0.9 (±0.5)

Relative binding energy (kcal/mol) was calculated with free energy at 0 mV as reference (alamI: -8.7 kcal/mol, alamT: -6.7 kcal/mol, HAFP: -7.9 kcal/mol, HIVFP: -8.5 kcal/mol, magainin: -6.9 kcal/mol, p25: -5.1 kcal/mol, WALP23: -23.8 kcal/mol). Standard deviation is given in parentheses. AlamI refers to the interfacial orientation, and alamT refers to the transmembrane orientation. The dipole potential energy term of all peptides at 400 mV was also calculated (alamI: -0.8 kcal/mol, alamT: -0.2 kcal/mol, HAFP: -3.2 kcal/mol, HIVFP: -4.9 kcal/mol, magainin: -0.6 kcal/mol, p25: -1.4 kcal/mol, WALP23: -0.6 kcal/mol)

This explanation, however, does not apply to HAFP, magainin, and p25. HAFP and magainin are almost parallel to the membrane. Therefore, the influence of the membrane dipole potential on the helix backbone dipole should be limited. Here, the change in binding affinity is due to ionic side chains. Magainin carries a total charge of +3 (four lysine and one glutamate residues). Although the dipole potential reaches its largest magnitude in the membrane interior, it also affects to a smaller extent the regions where the ionic side chains are. For example, a positively charged lysine NH3 group in magainin is located around 21 Å from the bilayer center, corresponding to 10 mV in case of a total ψ_d = 100 mV. This value, although small, is enough to cause a considerable interaction with the ionic side-chains of magainin. For the same reason, p25 with a total charge of +5, loses 3.7 kcal/mol of binding

affinity from 0 mV to 400 mV. HAFP has one aspartate residue and two glutamate residues, which gives the helix a total net charge of -3. Unlike magainin and p25, the interaction between the membrane dipole potential and the negatively charged helix should now be favored, which explains the 3.1 kcal/mol energy decrease from 0 mV to 400 mV for HAFP.

The smallest changes in binding energy are observed for the transmembrane peptides, WALP23 and alamT. WALP23 is uncharged and the helix backbone dipole is along the membrane normal. Because of symmetry, the interactions in the upper and lower leaflets essentially cancel out. As a result, the change in binding affinity is within statistical uncertainty. The alamT configuration is not entirely symmetric with respect to the membrane, but its interaction with the membrane dipole potential is also quite small. Unlike the neutral WALP23, alamT carries a net charge of -1 from its glutamate residue. The interaction between the membrane dipole potential and the negative charge provides additional stability to membrane binding, leading to a small favorable change in free energy with increasing dipole potential.

The values in Table 3.3 are averages from the MD simulations. As such, they are noisy and include contributions not only from the dipole potential-peptide interactions but also from changes in peptide configuration. Sometimes, there could even be secondary structure fluctuations, as was observed in the simulation of HIVFP and p25. In order to see how much the potential itself contributes to the binding energy, the average structure from the MD simulation at 0 mV for each helix was selected and single point energy calculations were performed on it at 0 mV, 100 mV, 200 mV, 300 mV, and 400 mV. Since everything else remains the same except the potential, the differences in energy show the effect of the dipole

potential only. The results are summarized in Figure 3.6 and exhibit the same pattern as that in Table 3.3. AlamT and WALP23 have the smallest energy change, while HIVFP has the largest

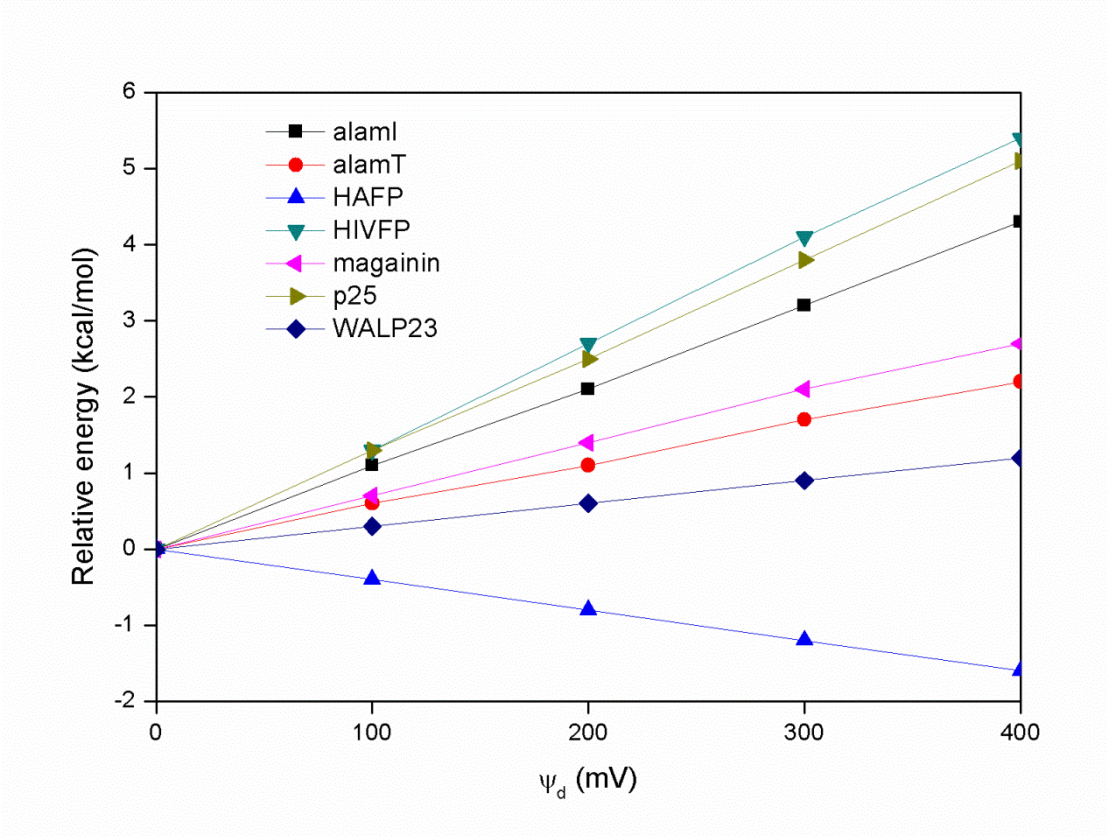

FIGURE 3.6 Relative energy as a function of ψ_d for the average structure from the MD simulation at 0 mV. Since the peptide structure remains the same, the energy difference is only related to the membrane dipole potential. The figure shows the same pattern as the binding energy in Table 3.3.

one. The values of alamI, magainin, and p25 are in between, changing by around 0.6-1.2 kcal/mol every 100 mV, and the binding of HAFP becomes more stable as ψ_d increases, consistent with Table 3.3. In order to check if the extra stability of HAFP is really caused by the interaction between the membrane dipole potential and ionic side-chains, aspartate and glutamate residues were replaced with neutral glycine residues. For the mutant peptide the energy increased by 3.4 kcal/mol from 0 mV to 400 mV, which confirms our explanation.

In experiments, by adding compounds such as phloretin, 6-KC, or cholesterol, or by changing lipid composition, ψ_d can be altered and the partition coefficient K_p or dissociation constant K_d can be measured (90-95). The binding free energy ΔG^o of the peptides to the membrane can then be deduced from K_p and K_d. Usually, however, the energy changes as a function of ψ_d is very small, sometimes close to experimental error. In addition, it is not clear that the observed differences are due to the change in the dipole potential or other factors. Despite this limitation, we will now survey the relevant experimental data and compare to our results.

Our simulations show that helices will lose binding affinity unless they carry a considerable amount of negative charge. The results from experiments are not conclusive. In a study of the interaction between p25 peptide and PC liposomes, Cladera and O'Shea found the dissociation constant K_d decreases from 4.0 ± 1.1 μM in the presence of phloretin to 3.1 ± 0.2 μM in the presence of 6-KC, corresponding to a decreasing ΔG^o with ψ_d (91). In a study of the interaction between HIV fusion peptide and PC/PE LUV, Buson and Cladera also reported a decreasing K_d as more 6-KC is added to the solution (94). As phloretin decreases and 6-KC increases the dipole potential, these experiments are not in agreement with our simulations. Others, however, are consistent with our findings. In a study of the interaction between the signal sequence of the Escherichia coli LamB protein with egg phosphatidylcholine (EPC), Voglino et al. reported a 0.1 kcal/mol and 2.4 kcal/mol ΔG^o increase by adding cholesterol and 6-KC respectively, both of which increase the magnitude of the membrane dipole potential (90). Similarly, in a study of the interaction of mitochondrial peptide rhodanese (MPR) and melittin with polyethylene glycol (PEG) LUV,

Allende et al. reported a 1.0 kcal/mol and 0.2 kcal/mol ΔG^o increase for MPR and melittin by adding 6-KC, and a 1.4 kcal/mol and 1.3 kcal/mol by adding cholesterol (93). Both of the above mentioned peptides are positively charged like p25. However, this loss of membrane affinity was attributed to factors other than the dipole potential in these studies. Voglino et al. pointed out that the ketone group of 6-KC will increase the hydrophilic thickness of the membrane interface by about 4 Å. As a result, fewer of the hydrophobic amino acids in the helix will be exposed to the low-dielectric acyl chain region of the bilayer, and the contribution of the hydrophobic energy to the binding free energy will decrease. Allende et al. proposed that addition of cholesterol increases the compressibility modulus of the bilayer. Therefore, to incorporate a peptide into the bilayer, extra work has to be done to increase the surface area of the bilayer to provide room for the peptide. Experimentally, it is very difficult to dissect these effects. Our results provide a theoretical basis for discussing the contribution of the membrane dipole potential to peptide membrane-bound structure and binding affinity.

3.4 Conclusions

We proposed a simple approach for implicit modeling of the dipole potential across lipid bilayers. The potential profile features a high value in the lipid hydrophobic core and a low value in water, joined together by a smooth curve around the headgroup region. The center and the width of the transition region were determined based on previous MD simulations with explicit lipids while its height ranges between 0 mV and 400 mV. The energy of interaction of a peptide with the dipole potential is then added as part of the solvation free energy in the implicit membrane model IMM1.

With this updated version of IMM1, we performed MD simulations on the helical peptides alamethicin, WALP23, HAFP, HIVFP, magainin, and p25. The influence of the membrane dipole potential on the helix orientation and binding energy was determined. For all helices, insertion of their N-termini to the cis leaflet of the bilayer leads to an unfavorable alignment between the backbone dipole and the potential (in addition to an also unfavorable interaction due to charge in case the N-terminus is protonated). Therefore, when the potential increases, the helix tilt angles increase as well, as observed for alamI, and to a smaller extent for HAFP, HIVFP, magainin, and p25. However, the interaction of the N-terminus with the trans leaflet is favorable, and leads to deeper membrane insertion and smaller tilt angle of alamT. The only peptide that gains membrane binding affinity with increasing dipole potential is HAFP, due to its net negative charge. All other peptides lose binding affinity with increasing dipole potential due to the interaction of either the backbone dipole or cationic side chains with the membrane dipole potential.

Chapter IV

INCLUSION OF LATERAL PRESSURE/CURVATURE STRESS EFFECTS IN IMPLICIT MEMBRANE MODELS

4.1 Introduction

Although spontaneously self-assembled phospholipid bilayers or biological membranes are tension-free, the local pressure within membranes is depth-dependent and can reach several hundred atmospheres (96, 97). This inhomogeneous distribution of the pressure along the membrane normal originates from the interaction between the membrane constituents and the balancing hydrophobic effect on exposure of the lipid chain to water at the polar-apolar interface. The resulting lateral pressure profile features two positive pressure peaks in the acyl chain and headgroup regions, and a negative pressure peak at the interface (96, 97).

The microscopic lateral pressure is related to the macroscopic elasticity of the membrane through its moments along the normal. The first moment is related to the mean curvature modulus k_c and spontaneous curvature c_o (98),

$$P_1 = \int z p(z) dz = k_c c_o \tag{4-1}$$

k_c can be experimentally determined by the methods of thermal fluctuation of bending (99, 100), pipette-aspiration (101), or dual-solvent stress (102, 103). The second moment is related to the Gaussian curvature modulus $\bar{k}_c$ (98),

$$P_2 = \int (z-\delta)^2 \, p(z) dz = -\bar{k}_c \tag{4-2}$$

In Eq. 4-2, δ is the position of the neutral plane (the plane of inextension), which is usually found to lie close to the interface (104-106). $\bar{k}_c$ can be measured by the response of cubic

Q_{II}-phase dimensions to varying water content (104), or observation of L_{α}-Q_{II} phase coexistence (106). Eq. 4-1 and Eq. 4-2 provide a link between the lateral pressure profile and the curvature stress of the membrane.

Although the lateral pressure is widely accepted as an inherent property of lipid membranes, its direct measurement is not yet possible. Indirect methods include the use of ^{2}H-NMR (107) and fluorescent probes (108), however, the results are not reliable due to uncertainties in the interpretation of the experiments. As an alternative, lateral pressure data have been obtained by theoretical and computational methods such as mean-field theory (MFT) (109-116) and molecular dynamics (MD) simulations (117-128). The MD simulations enable the calculation of the pressure profile across the entire bilayer, by representing the lipids explicitly with atomistic (117-126) or coarse-grained (CG) models (127, 128). The results, however, do not agree very well with each other, indicating that the calculation is sensitive to the simulation protocol and/or the force field (119). The best known MFT studies are those of Cantor (113-116). The MFT approach has the advantage of not being subject to statistical errors due to inadequate sampling. However, the assumption of a uniformly packed hydrophobic core of the bilayers may be problematic (118). Other computational approaches, such as dissipative particle dynamics (129) and Monte Carlo simulations (130), have also been used to obtain the pressure profile.

The lateral pressure is affected by the variations in lipid composition. Cantor investigated the influence of chain unsaturation and showed that, due to the difference in the packing of the chains, double bonds close to the headgroup have much stronger effect on the lateral pressure than those at the end of the chain (115). In addition, broadly distributed

double bonds lead to broad pressure distribution as well without significantly changing the thickness of the bilayer. This study also showed that even small quantities of cholesterol can cause significant changes to the pressure profile, characterized by a position shift toward the membrane interior and a maximum magnitude decrease adjacent to the interface. This effect is opposite to that of adding small solutes such as short chain alcohols or general anesthetics. As for the influence of headgroups, not yet confirmed by computations, experiments suggest that conical-shaped non-bilayer lipids may induce a pressure decrease in the headgroup region and an increase in the acyl chain region (131).

One of the reasons that the study of membrane lateral pressure has attracted great interest is that the variation in lipid composition could influence the conformation and function of membrane proteins and peptides. For example, higher conductance states of the alamethicin ion channel were found to be more probable in dioleoylphosphatidylethanolamine (DOPE) than in dioleoylphosphatidylcholine (DOPC) (132), perhaps due to the preference of DOPE for the oligomeric state of the peptide (133). *E. coli* leader peptidase, an integral membrane protein crucial for the protein secretion pathway, was shown to have a preference for non-bilayer lipids over phosphatidylcholine (PC) and phosphatidylglycerol (PG) upon insertion into lipid monolayers (134). The transition free energy of rhodopsin between the meta-I and meta-II states was found to exhibit a linear dependence on the spontaneous curvature of DOPC/DOPE mixtures (135). Finally, the activity of peripheral membrane proteins such as protein kinase C (136, 137), phospholipase A2 (138), and CTP: phosphocholine cytidylyltransferase (138, 139) was also reported to be affected by non-bilayer lipids.

In recent years implicit solvation models have increasingly been applied to MD simulation of peptides in membranes due to their computational efficiency (10). These models have been extended to account for the effect of surface charge (11, 28-30), transmembrane voltage (140), aqueous pores (141-143), and recently membrane dipole potential (144). Despite its importance, the lateral pressure has not yet been incorporated into implicit membrane models. As a result, it is not possible to model the effects of lipid composition, such as, for example, the change from PC to PE. Since the lateral pressure profile has a well-defined shape across lipid bilayers, in this study we represent the pressure as an external field, and incorporate it into the IMM1 implicit membrane model (10). The new model is used to study the influence of peptide/lipid molar ratio and lipid composition on the membrane binding energy and configuration of the peptides alamethicin, melittin, cyclotide kalata B1 (KB1), 18A, and $^{KK}pL_{15}$.

4.2 Theory

Upon peptide binding, the total area A_B of a bilayer is given by Ref. 96

$$A_B = n_L a_L + n_P a_P \tag{4-3}$$

where a_L is the area per lipid, a_P is the peptide cross-sectional area, and n_L and n_P are the moles of lipid and peptide respectively. From Eq. 4-3 we get

$$n_L \left(\frac{\partial a_L}{\partial n_P} \right)_{n_L} = \left(\frac{\partial A_B}{\partial n_P} \right)_{n_L} - a_P \tag{4-4}$$

Based on Eq. 4-4, if the bilayer expands by the full peptide cross-sectional area ($\left(\partial A_B / \partial n_P\right)_{n_L} = a_P$), there is no compression to the lipids. On the other hand, if the bilayer

does not expand at all ($(\partial A_B / \partial n_P)_{n_L} = 0$), the lipids are compressed by the full peptide cross-sectional area (96). Since the true expansion of a bilayer is hard to estimate and depends on the experimental situation, here we write $(\partial A_B / \partial n_P)_{n_L}$ as

$$\left(\frac{\partial A_B}{\partial n_P}\right)_{n_L} = \lambda a_P \tag{4-5}$$

where λ is defined as the expansion coefficient, which can range from 0 to 1. In this study it is treated as a free parameter, tentatively set to 0.5. From Eq. 4-4 and Eq. 4-5, we get

$$n_L\left(\frac{\partial a_L}{\partial n_P}\right)_{n_L} = -(1-\lambda)a_P \tag{4-6}$$

Since a_P varies along the membrane normal, Eq. 4-6 has to be re-written as

$$n_L\left(\frac{\partial a_L(z)}{\partial n_P}\right)_{n_L} = -(1-\lambda)a_P(z) \tag{4-7}$$

To insert a peptide into the bilayer at infinite dilution (infinitesimal peptide/lipid molar ratio n_P / n_L), one needs to do work against the pressure profile (96, 113),

$$W = -\int n_L\left(\frac{\partial a_L(z)}{\partial n_P}\right)_{n_L} p(z)dz \tag{4-8}$$

By plugging Eq. 4-7 into Eq. 4-8, we get

$$W = (1-\lambda)\int a_P(z)p(z)dz \tag{4-9}$$

When λ = 0 (the bilayer does not expand at all), Eq. 4-9 can be simplified as $W = \int a_P(z)p(z)dz$, which is consistent with Eq. 2 in Ref. 114.

To calculate W in Eq. 4-9 in our model, a bilayer is evenly divided into slabs from the center (z = 0 Å) to a position in water (z = 30 Å) where the pressure is taken to be 0. The thickness of the slabs is set to h = 0.1 Å, a value much smaller than the size of any atom. So within each slab, both a_P and p can be treated as approximately independent of z, and

Eq. 4-9 is then written as

$$W = h(1-\lambda)\sum_k a_{P,k}\, p_k \tag{4-10}$$

where k runs over all slabs.

At finite n_P / n_L, one has to take into account that the lateral pressure profile itself is affected by the presence of peptides. Thus, the lateral pressure within each slab is a function of the peptide cross-sectional area (96), and Eq. 4-10 has to be re-written as

$$W = h(1-\lambda)\sum_k \int_0^{a_{P,k}} p_k\left(a_{P,k}\right) da_{P,k} \tag{4-11}$$

The explicit form of $p_k\left(a_{P,k}\right)$ can be obtained based on thermodynamics. At constant temperature the relation between the lateral pressure p_k and total volume of lipids $V_{L,k}$ at slab k upon peptide binding is given by

$$K_{A,k} = -V_k\left(\frac{\partial p_k}{\partial V_{L,k}}\right)_T \tag{4-12}$$

where $K_{A,k}$ is the compressibility modulus of the slab. Integration of Eq. 4-12 gives

$$p_k - p_k^o = -K_{A,k} \ln\frac{V_{L,k}}{V_{L,k}^o} = -K_{A,k} \ln\left(1+\frac{\Delta V_{L,k}}{V_{L,k}^o}\right) \tag{4-13}$$

where p_k^o and $V_{L,k}^o$ are the lateral pressure and total volume of lipids in the pure bilayer, and $\Delta V_{L,k} = V_{L,k} - V_{L,k}^o$. If the stress caused by peptide binding is small, Eq. 4-13 can be approximated as

$$p_k - p_k^o = -K_{A,k}\frac{\Delta V_{L,k}}{V_{L,k}^o} \tag{4-14}$$

Since the stress is in-plane, we have

$$\frac{\Delta V_{L,k}}{V_{L,k}^o} = \frac{\Delta A_{L,k}}{A_{L,k}^o} \tag{4-15}$$

Noting that $\Delta A_{L,k} = \int n_L\left(\partial a_{L,k} / \partial n_P\right)_{n_L} dn_P = -(1-\lambda) n_P a_{P,k}$ and $A_{L,k}^o = n_L a_L^o$, Eq. 4-15 can

be written as

$$\frac{\Delta V_{L,k}}{V_{L,k}^o} = -(1-\lambda)\frac{n_P a_{P,k}}{n_L a_L^o} \tag{4-16}$$

In Eq. 4-16 $a_{P,k}$ is the peptide cross-sectional area, and a_L^o is the area per lipid in the pure bilayer. By plugging Eq. 4-16 into Eq. 4-14, we get

$$p_k = p_k^o + (1-\lambda)\frac{K_{A,k}}{a_L^o}\left(\frac{n_P}{n_L}\right)a_{P,k} \tag{4-17}$$

Based on Eq. 4-17, Eq. 4-11 can be written as

$$W = h(1-\lambda)\sum_k p_k^o a_{P,k} + \frac{h(1-\lambda)^2}{2a_L^o}\left(\frac{n_P}{n_L}\right)\sum_k K_{A,k} a_{P,k}^2 \tag{4-18}$$

The second term on the right hand side of Eq. 4-18 is caused by the lateral compression to lipids upon peptide binding at finite n_P / n_L. The same term, with λ = 0, was derived in a different way in Ref. 155. In summary, Eq. 4-18 is the discrete form of the work against the lateral pressure for inserting a peptide into a bilayer. It extends the equation given by Cantor (113) in two ways: (i) it takes into consideration of the pressure change caused by the compression to lipids upon peptide binding at finite n_P / n_L; (ii) it takes into consideration the bilayer area expansion by introducing an expansion coefficient. Since Eq. 4-14 is inaccurate at high n_P / n_L, in our simulations W was calculated based on Eq. 4-13, which gives Eq. 4-19.

$$W = h(1-\lambda)\sum_k p_k^o a_{P,k} + h(1-\lambda)\sum_k \left(\frac{K_{A,k}}{\beta}(1-\beta a_{P,k})(\ln(1-\beta a_{P,k})-1)+1\right) \tag{4-19}$$

where $\beta = ((1-\lambda)/a_L^o)(n_P / n_L)$.

4.3 Methods

4.3.1 The peptide cross-sectional area

To obtain $a_{P,k}$ in Eq. 4-18, we make the assumption that the cross-sectional area of a peptide can be calculated by summing over individual atoms,

$$a_{P,k} = \sum_i a_i^k \tag{4-21}$$

where a_i is the cross-sectional area of atom i, and i runs over all atoms occupying slab k. Overlaps between bonded atoms and intersticial spaces are taken into account in an approximate fashion. Treating each atom as an ideal sphere, the cross-sectional area is a function of the distance between the center of the atom (z_i) and the position of the slab plane ($z_k^{'}$),

$$a_i^k = \pi\left(R_i^2 - \left| z_i - z_k^{'} \right|^2 \right), \left(\left| z_i - z_k^{'} \right| \le R_i \right) \tag{4-22}$$

In Eq. 4-22 R_i is the radius of the atom, which is calculated by using the atomic volume V_i from the IMM1 solvation parameters (10) ($R_i = \left(3V_i / 4\pi\right)^{1/3}$) and is then empirically increased by 10% to account for the empty space between atoms.

By plugging Eq. 4-22 into Eq. 4-21 and doing the calculation for all slabs, a cross-sectional area profile along the membrane normal can be obtained. As a test, the calculation was performed on transmembrane and interfacial $(GLY)_{22}$ helix and the result is given in Fig. 4.1. The highest areas of 300 $Å^2$ and 45 $Å^2$ for the transmembrane and interfacial orientations are very close to the 270 $Å^2$ and 53 $Å^2$ calculated with an ideal helix model (2.3 Å for helix radius, 1.8 Å for the average radius of backbone atoms, and 1.5 Å rise per residue along the helix axis).

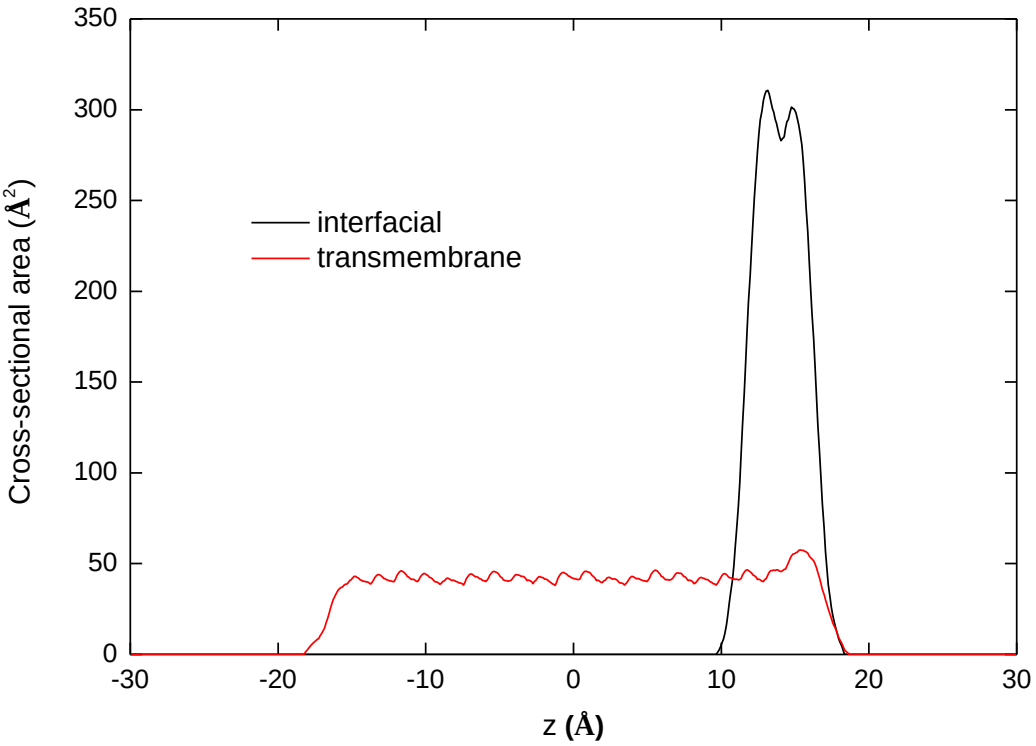

FIGURE 4.1 The cross-sectional area of transmembrane and interfacial orientations of an ideal $(GLY)_{22}$ α-helix calculated as a sum of atomic contributions.

4.3.2 Fitting the lateral pressure profile of the DOPC bilayer

Since the lateral pressure profile of pure DOPC bilayer has been computed by several explicit MD simulations, a simple way to get p_k^o in Eq. 4-18 would be to use these data directly. For more flexibility, however, and to impose consistency with experimental measurements, we fit the existing pressure distribution with an analytical function. The parameters controlling the position and width of the peaks and the magnitude at the interface are estimated by using the pressure profile from explicit MD simulations. The parameters for controlling the magnitude in the acyl chain and headgroup regions are then calculated based on Eq. 4-1 and Eq. 4-2.

Since the lateral pressure originates from the repulsion in the acyl chain and headgroup regions and the cohesive tension at the interface (131), we decompose the pressure within a

monolayer leaflet into three Gaussian components,

$$p^o(a,b,c,z) = a \cdot \exp\left(-\frac{(z-b)^2}{c^2}\right) \tag{4-23}$$

where a, b, and c are the parameters controlling the magnitude, position, and width of the pressure, respectively, and vary in each region. Based on Eq. 4-23, the first and second moments are given by

$$P_1 = m_1 a \tag{4-24}$$

$$P_2 = m_2 a \tag{4-25}$$

where $m_1 = \sqrt{\pi} bc$ and $m_2 = \sqrt{\pi} c\left((b-\delta)^2 + c^2/2\right)$. The moments of the whole leaflet are linear combinations of the three components,

$$P_1 = m_{1A} a_A + m_{1I} a_I + m_{1H} a_H \tag{4-26}$$

$$P_2 = m_{2A} a_A + m_{2I} a_I + m_{2H} a_H \tag{4-27}$$

where subscripts A, I, and H denote the acyl chain, interface, and headgroup respectively. By plugging Eq. 4-26 and Eq. 4-27 into Eq. 4-1 and Eq. 4-2, we get

$$\begin{pmatrix} m_{1A} & m_{1I} & m_{1H} \\ m_{2A} & m_{2I} & m_{2H} \end{pmatrix} \begin{pmatrix} a_A \\ a_I \\ a_H \end{pmatrix} = \begin{pmatrix} k_c c_o \\ -\bar{k}_c \end{pmatrix} \tag{4-28}$$

or

$$\begin{pmatrix} a_A \\ a_H \end{pmatrix} = \begin{pmatrix} m_{1A} & m_{1H} \\ m_{2A} & m_{2H} \end{pmatrix}^{-1} \begin{pmatrix} k_c c_o - m_{1I} a_I \\ -\bar{k}_c - m_{2I} a_I \end{pmatrix} \tag{4-29}$$

In Eq. 4-29, the pressure profile from Ollila's simulation (122) was used to estimate m_{1A}, m_{2A}, m_{1I}, m_{2I}, m_{1H}, m_{2H}, and a_I. k_c, $\bar{k}_c$, and c_o were taken from experiments (145), in which $k_c = 4.0 \times 10^{-20} J$ and $\bar{k}_c = -0.8 k_c$. Finally, a_A and a_H can be calculated by solving Eq. 4-29, and then the whole pressure profile of the monolayer leaflet is given by

$$p^o(z) = p^o(a_A, b_A, c_A, z) + p^o(a_I, b_I, c_I, z) + p^o(a_H, b_H, c_H, z) \quad (4\text{-}30)$$

For a symmetric bilayer, the two leaflets will have the same lateral pressure profile. Extension to asymmetric bilayers is straightforward.

4.3.3 The lateral pressure profile of mixed DOPC/DOPE bilayers

For mixed DOPC/DOPE monolayers, the spontaneous curvature c_o is a function of the mole fraction of DOPE (χ) (103),

$$c_o = (1-\chi)c_o^{DOPC} + \chi c_o^{DOPE} \quad (4\text{-}31)$$

where c_o^{DOPC} and c_o^{DOPE} are the spontaneous curvatures of DOPC and DOPE monolayers, whose values are -0.0066 Å^{-1} and 0.0431 Å^{-1}, respectively (97). c_o is then plugged back into Eq. 4-29 and the corresponding a_A and a_H can be calculated. The reason that in Eq. 29 the same parameters except a_A, a_H, and c_o are used for DOPC and DOPE is the following: (i) both lipids have the same type of acyl chains, which makes it reasonable to assume that the position and width of the pressure peaks do not change too much; (ii) the pressure at the interface is characterized by the contact of hydrocarbon with bulk water and is much the same for all lipids (97); (iii) experiments give similar k_c for DOPC and DOPE monolayers (145). In Fig. 4.2, the lateral pressure profiles at χ = 0, 0.2, 0.4, 0.6, and 0.8 are plotted. It can be seen that the non-bilayer DOPE increases the pressure in the acyl chain region and decreases it in the headgroup region, as suggested by both fluorescence (108) and ^{2}H-NMR experiments (146-148).

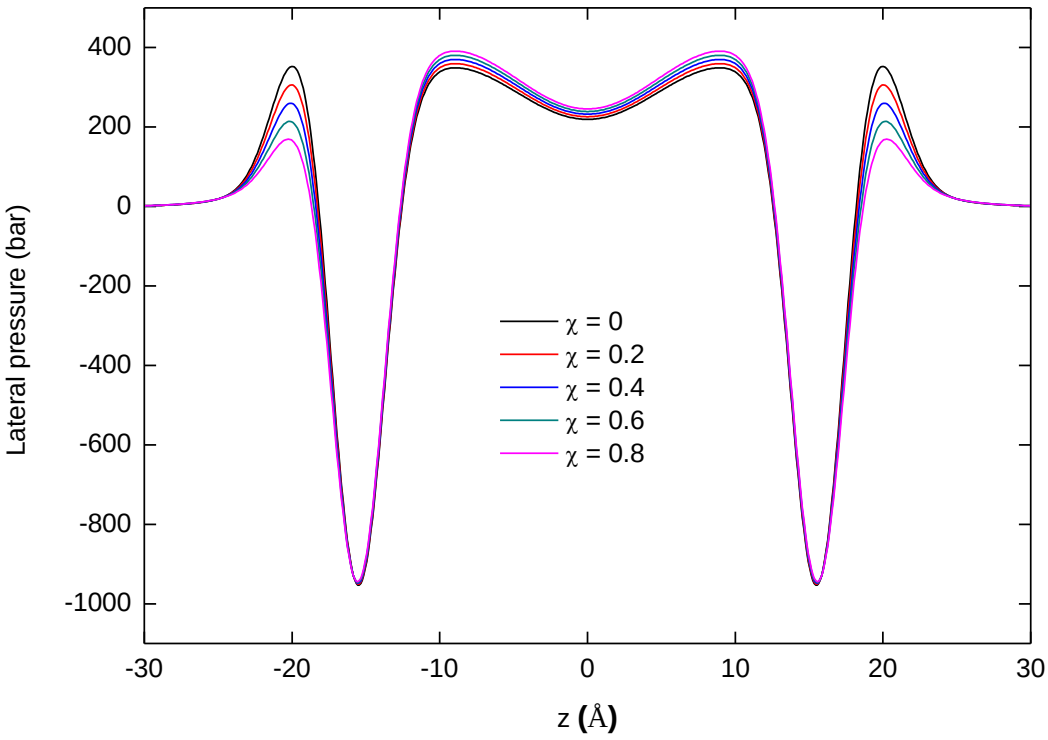

FIGURE 4.2 The lateral pressure profile of a mixed DOPC/DOPE bilayer at different mole fractions of DOPE.

4.3.4 The compressibility modulus and total energy of peptide binding

In this model, the compressibility modulus is treated as a constant along the membrane normal, and $K_{A,k}$ in Eq. 4-18 is assumed to be

$$K_{A,k} = \frac{K_A}{d} \tag{4-32}$$

where K_A is the compressibility modulus of the bilayer, set to 240 mN/m for DOPC (105), and d is the bilayer thickness including both hydrocarbon (25.4 Å) and headgroup regions (20 Å). Since experiments give similar K_A, A_L^o, and bilayer thickness for DOPC and DOPE (Table 4.1), for convenience the same parameters are also used for DOPE. From Eq. 4-18

TABLE 4.1 Experimental parameters of DOPC and DOPE bilayers

	K_A (mN/m)*	k_c (10^{-20} J)†	$\bar{k}_c$ (J)†	c_o (Å^{-1})†	d_l (Å)‡	a_L^o (Å^2)§
DOPC	240	4.0	$-0.8\,k_c$	-0.0066	36	70
DOPE	240	4.5		-0.0431	37	65

*K_A from Table 1 of Rawicz et al (105), which is all about 240 mN/m for more than 10 lipids. Therefore, the value of 240 mN/m is used for both DOPC and DOPE in this study. †See Marsh (97). These values are for monolayers. ‡d_l from Table 1 of Rand and Parsegian (149), which is the distance between the center of the phosphate groups. §See Rand and Parsegian (149).

and Eq. 4-32, we get

$$W = E^{LAT} + E^{COM} = h(1-\lambda)\sum_k p_k^o a_{P,k} + \frac{h(1-\lambda)^2 K_A}{2da_L^o}\left(\frac{n_P}{n_L}\right)\sum_k a_{P,k}^2 \qquad (4\text{-}33)$$

In Eq. 4-33, the first term is represented as E^{LAT} since it is related to the lateral pressure of the pure bilayer, and the second term is represented as E^{COM} since it is related to the compressibility modulus. The total energy of peptide binding to the bilayer is then given by

$$E = E^{IMM1} + E^{LAT} + E^{COM} \qquad (4\text{-}34)$$

where E^{IMM1} is the standard IMM1 energy.

4.3.5 Molecular dynamics simulations

MD simulations were carried out at 300 K using the CHARMM program (33). Membrane and water were implicitly represented with IMM1. Five peptides were simulated: alamethicin,

TABLE 4.2 Sequences of the peptides studied

Alamethicin	Ac-UPUAUAQUVUGLUPVUUEQF-OH
Melittin	Ac-GIGAVLKVLTTGLPALISWIKRKRQQ-NH_2
KB1	Ac-CGETCVGTCNTPGCTCSWPVCTRNGLPV-NH_2
18A	Ac-DWLKAFYDKVAEKLKEAF-NH_2
$^{KK}pL_{15}$	Ac-KKLLLLLLLDWLLLLLLLLKK-NH_2

melittin, KB1, 18A, and $^{KK}pL_{15}$, whose sequences are given in Table 4.2. The simulations were done in a zwitterionic (neutral) bilayer, whose hydrocarbon thickness is set to 25.4 Å corresponding to the DOPC bilayer (150). The initial structures of the peptides were generated by CHARMM based on their sequences except KB1, for which the crystal structure was used. In order to study the influence of peptide/lipid molar ratio on peptide binding, simulations were performed on alamethicin in pure DOPC bilayer from n_P / n_L = 0.01 to 0.10 in 0.01 increments. In order to study the influence of non-bilayer lipids, simulations were performed on all peptides in mixed DOPC/DOPE bilayers at χ = 0, 0.2, 0.4, 0.6, and 0.8. In the second study, n_P / n_L = 0.01 was used for all peptides.

Each simulation run lasted 10 ns, and the average structures and energies of the last 5 ns were taken for analysis. The binding energy of the peptides was estimated as the average effective energy difference in membrane and water environments for the conformational ensemble generated by the membrane simulation,

$$E^{BINDING} = \frac{1}{N}\sum_{i=1}^{N}\left(E_i^{MBR} - E_i^{WAT}\right) \tag{4-35}$$

where E_i^{MBR} and E_i^{WAT} are the effective energy in membrane and in water respectively, and i runs through N = 2500 conformations saved at equal intervals within the last 5 ns of the

simulation.

4.4 Results

4.4.1 Binding of alamethicin to a DOPC bilayer at various peptide/lipid molar ratios

Alamethicin is a 20-amino acid helical peptide forming voltage-gated ion channels in lipid bilayers (151). Previous MD simulations with IMM1 showed that alamethicin can bind lipid bilayers at two orientations, one interfacial and one more deeply inserted, almost transmembrane. The binding energy of the former is 1-2 kcal/mol lower than that of the latter (140, 144). These simulations also showed that the N-terminus of the interfacial orientation is slightly tilted and buried under the interface, while the tilt angle between the transmembrane orientation and bilayer normal is around 30^{o}.

In this study, alamethicin was initially placed both parallel to the bilayer at the interface and inserted perpendicular to the bilayer. The peptide/lipid molar ratio n_P / n_L was first set to 0.01. Both interfacial and transmembrane binding were observed in the simulation (Fig. 4.3), however, it can be seen from the figure that the N-terminus of our interfacial orientation is no longer tilted. Also, it was found that with the lateral pressure added to IMM1, the interfacial orientation is significantly stabilized, with binding energy now 8 kcal/mol lower than that of the transmembrane orientation (Table 4.3).

In order to investigate the influence of peptide/lipid molar ratio on the binding, we increased n_P / n_L from 0.01 to 0.10 at 0.01 increments, and repeated the simulation at each

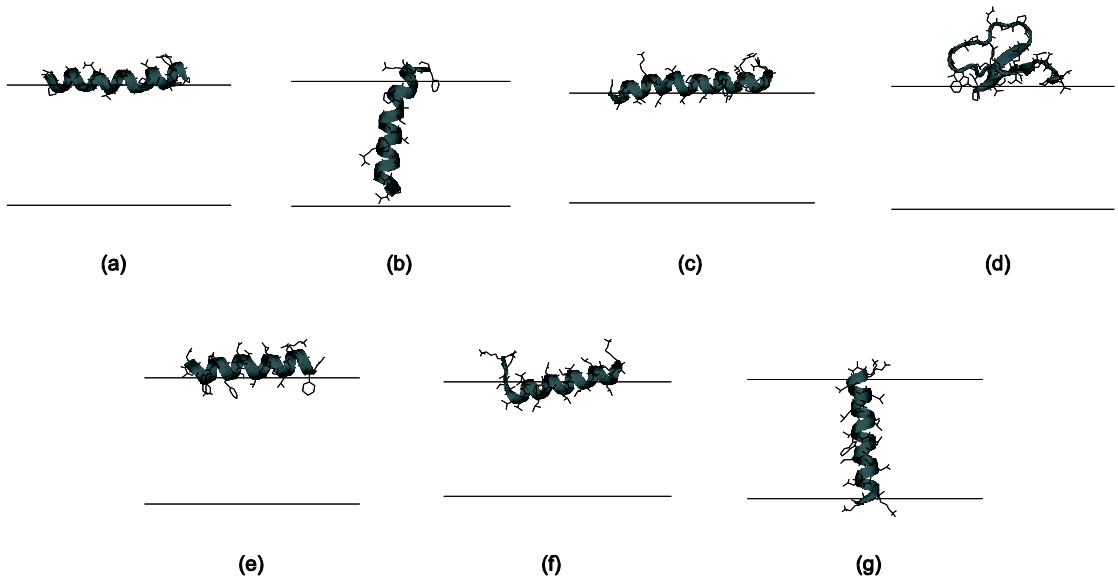

FIGURE 4.3 The average configuration of (a) interfacial alamethicin, (b) transmembrane alamethicin, (c) melittin, (d) KB1, (e) 18A, (f) interfacial $^{KK}pL_{15}$, and (g) transmembrane $^{KK}pL_{15}$ at n_P / n_L = 0.01 and χ = 0. The structures do not change significantly with n_P / n_L or χ. The lines denote the hydrophobic boundary of the bilayers.

n_P / n_L. Since the transmembrane orientation has significantly higher relative binding energy, the peptide easily moves to the interfacial orientation in most of the simulations even though it was initially placed perpendicular to the bilayer. Therefore, to obtain energy data for the transmembrane configuration, harmonic constraints were applied to the Cα atoms using the n_P / n_L = 0.01 structure as a reference. This way the binding energy of both orientations as a function of n_P / n_L was calculated and reported in Table 4.3. It can be seen from the table that the binding energy increases with n_P / n_L for both interfacial and transmembrane orientations. However, the increase is much faster for the former. Therefore, we expect equilibrium to shift from the interfacial to transmembrane orientation as n_P / n_L increases. Experimentally, a transition from interfacial to transmembrane has been observed for many

TABLE 4.3 Binding energy (kcal/mol) of alamethicin at various peptide/lipid molar ratios

n_P / n_L	ΔE^{IMM1}	ΔE^{LAT}	ΔE^{COM}	$E^{BINDING}$
0.01	-7.6/-7.0	1.5/-7.1	0.0/0.1	-6.1/-14.0
0.02	-7.5/-7.0	1.5/-7.2	0.1/0.3	-5.9/-13.9
0.03	-7.5/-7.1	1.5/-7.0	0.1/0.4	-5.9/-13.8
0.04	-7.6/-7.0	1.5/-7.1	0.2/0.5	-5.9/-13.6
0.05	-7.5/-7.1	1.5/-7.1	0.2/0.7	-5.8/-13.5
0.06	-7.6/-7.1	1.5/-7.0	0.3/0.8	-5.9/-13.3
0.07	-7.6/-7.2	1.5/-7.1	0.3/1.0	-5.8/-13.2
0.08	-7.6/-7.2	1.5/-7.0	0.3/1.1	-5.8/-13.1
0.09	-7.5/-7.2	1.5/-7.0	0.4/1.2	-5.7/-13.0
0.10	-7.6/-7.2	1.5/-7.0	0.4/1.4	-5.6/-12.8

The first number is for the transmembrane orientation and the second for the interfacial orientation. $E^{BINDING} = \Delta E^{IMM1} + \Delta E^{LAT} + \Delta E^{COM}$, where Δ denotes the transfer from water to membrane. The average standard deviation is about 0.1 kcal/mol.

antimicrobial peptides, including alamethicin (152-154). This transition was attributed to the thinning of the bilayer caused by the interfacial binding of the peptides (155). Although the shift we observed is in agreement with experiment, experiment gives a threshold concentration of 0.02 for alamethicin binding on DPhPC bilayer (156), while we are not able to observe the transition on DOPC bilayer from n_P / n_L = 0.01 to 0.10. This may be due to the fact that IMM1 has been parameterized without the inclusion of a lateral pressure term (see Discussion).

4.4.2 Binding of peptides to mixed DOPC/DOPE bilayers

Alamethicin

The effect of DOPE mole fraction on the binding energy of alamethicin was investigated separately for interfacial and transmembrane configurations. As before, harmonic constraints on the Cα atoms were employed to keep alamethicin transmembrane. The binding energy as a function of χ is plotted in Fig. 4.4A (the contribution of all components is given in Table 4.4). From the figure it can be seen that for the interfacial orientation, the binding energy barely changes. For the transmembrane orientation, however, the binding energy increases with χ. This is consistent with experiment, which reported that in mixed DOPC/DOPE bilayers the binding free energy of transmembrane alamethicin increases linearly with the mole fraction of DOPE (133). From $\chi = 0$ to 0.6 our binding energy for the transmembrane orientation increases by 0.5 kcal/mol, which is slightly smaller than the experimental value of 0.8 kcal/mol.

Since the binding energy is an average from MD simulations, it is noisy and includes contributions not only from changes in lipid composition, but also changes in peptide configuration. In order to see how much the lipid composition alone contributes to the binding energy, energy calculations were performed on the average binding structure of the peptide from $\chi = 0$ to 0.8. The result is given in Fig. 4.4B and is consistent with that obtained using average energies.

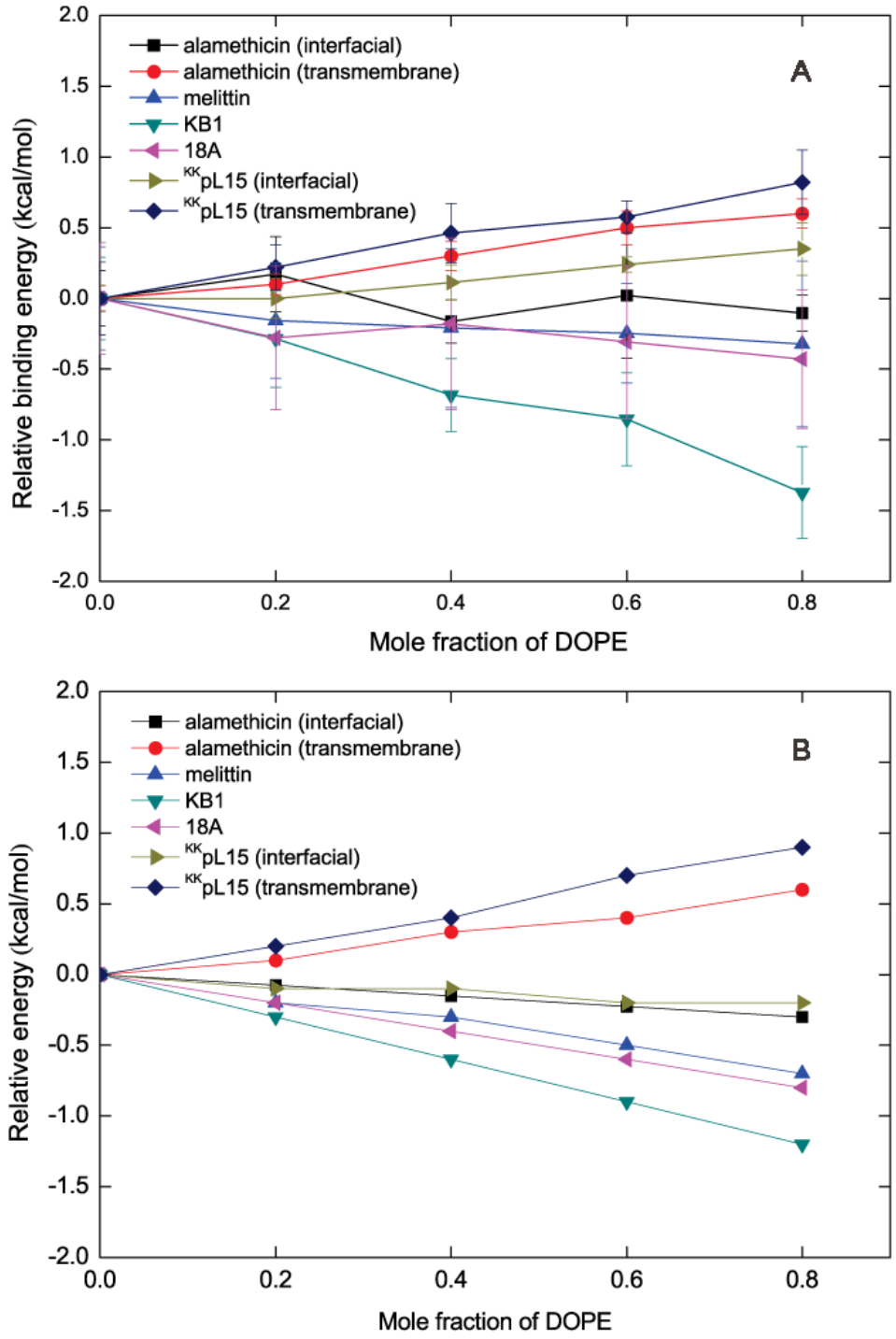

FIGURE 4.4 (A) The relative binding energy of the peptides on mixed DOPC/DOPE bilayers at various mole fractions of DOPE. (B) The relative energy calculated with the average binding structures obtained at $n_P / n_L = 0.01$ and $\chi = 0$.

Melittin

Melittin, a 26-amino acid helical peptide, is the main proteinaceous constituent of the honeybee venom. The orientation as well as insertion depth of melittin upon binding to membranes has been the subject of extensive debate. Experiments under various conditions suggest either a transmembrane or an interfacial orientation (157, 158). Nevertheless, it is likely that an interfacial binding is more reasonable for neutral bilayers with the hydrophobic thickness of DOPC (10). Therefore, at the beginning of our simulation melittin was placed parallel to the bilayer at the interface.

During the simulations melittin stayed primarily at the interface, with the C-terminus slightly becoming unstructured and moving toward the water, as shown in Fig. 4.3. Fig. 4.4 shows that the binding energy of melittin decreases by a very small amount (around 0.3 kcal/mol) from $\chi = 0$ to 0.8. Experiment reported that melittin binds with similar affinity to liquid crystalline DEPC and DEPE vesicles, albeit at different temperatures, while in the gel phase binding to DEPE is much weaker than to DEPC (159).

Cyclotide kalata B1

The cyclotides are a large family of peptides from plants, among which the prototypic cyclotide kalata B1 (KB1) is the most well studied and has been shown to bind (160) and disrupt phospholipid bilayers by a pore-forming mechanism (161). The cyclic knotted

TABLE 4.4 Binding energy (kcal/mol) at various mole fractions of DOPE

		$\chi = 0$	$\chi = 0.2$	$\chi = 0.4$	$\chi = 0.6$	$\chi = 0.8$
Alamethicin (interfacial)	ΔE^{IMM1}	-6.9	-6.7	-7.0	-6.5	-6.7
	ΔE^{LAT}	-7.1	-7.3	-7.3	-7.6	-7.6
	ΔE^{COM}	0.1	0.1	0.1	0.2	0.1
	$E^{BINDING}$	-14.0	-13.8	-14.1	-14.0	-14.1
Alamethicin (transmembrane)	ΔE^{IMM1}	-7.6	-7.6	-7.6	-7.6	-7.6
	ΔE^{LAT}	1.5	1.6	1.8	1.9	2.1
	ΔE^{COM}	0.0	0.0	0.0	0.0	0.0
	$E^{BINDING}$	-6.1	-6.0	-5.8	-5.6	-5.5
Melittin	ΔE^{IMM1}	-13.2	-13.1	-13.0	-12.8	-12.7
	ΔE^{LAT}	-8.1	-8.4	-8.6	-8.8	-9.0
	ΔE^{COM}	0.1	0.2	0.2	0.2	0.2
	$E^{BINDING}$	-21.2	-21.3	-21.4	-21.4	-21.5
KB1	ΔE^{IMM1}	-0.4	-0.2	-0.4	-0.4	-0.4
	ΔE^{LAT}	-5.4	-5.9	-6.1	-6.2	-6.8
	ΔE^{COM}	0.1	0.2	0.1	0.1	0.1
	$E^{BINDING}$	-5.6	-5.9	-6.3	-6.5	-7.0
18A	ΔE^{IMM1}	-5.0	-5.1	-4.9	-4.8	-4.8
	ΔE^{LAT}	-6.8	-7.0	-7.1	-7.3	-7.5
	ΔE^{COM}	0.1	0.1	0.2	0.1	0.2
	$E^{BINDING}$	-11.7	-11.9	-11.8	-12.0	-12.1
$^{KK}pL_{15}$ (interfacial)	ΔE^{IMM1}	-26.1	-26.0	-25.7	-25.3	-24.9
	ΔE^{LAT}	-3.7	-3.8	-4.0	-4.3	-4.5
	ΔE^{COM}	0.2	0.2	0.2	0.2	0.2
	$E^{BINDING}$	-29.6	-29.6	-29.5	-29.4	-29.3
$^{KK}pL_{15}$ (transmembrane)	ΔE^{IMM1}	-28.3	-28.3	-28.3	-28.4	-28.3
	ΔE^{LAT}	2.9	3.0	3.2	3.5	3.7
	ΔE^{COM}	0.1	0.1	0.1	0.1	0.1
	$E^{BINDING}$	-25.4	-25.2	-24.9	-24.8	-24.6

structure of KB1 is stabilized by three di-sulfide bridges, and binds to membranes via two hydrophobic loops (162). The starting structure of KB1 was taken from the PDB bank (PDB entry: 1NB1) and was placed with the hydrophobic loops at the interface.

During the simulation, the peptide stayed as the cyclic structure at the interface, with the two hydrophobic loops anchoring superficially into the hydrophobic core of the bilayer (Fig. 4.3). The C-terminus of the peptide is more flexible than the N-terminus. It can be seen from Fig. 4.4 that the binding energy of KB1 decreases by the largest amount among all peptides, and from χ = 0.1 to 0.2 the energy decreases by about 0.2 kcal/mol. In a surface plasmon resonance (SPR) experiment it was reported that the peptide/lipid molar ratio increases from 0.08 to 0.15 as the mole percentage of DOPE in DOPC vesicles increases from 10% to 20% (163). From this one can deduce a binding free energy decrease of about 0.35 kcal/mol. The authors attribute the affinity for PE to specific interactions with the headgroup, but we find that a large portion of the affinity increase can be explained by lateral pressure/curvature stress effects.

18A

18A is a designed amphipathic peptide of 18 residues. CD experiments indicated that the peptide adopts mainly helical structure in membranes, and ^{2}H-NMR showed that the insertion of the peptide occurs at the membrane interface (164). Based on this, the peptide was built as an ideal α-helix and placed initially parallel to the bilayer at the interface.

During the simulations the helical structure of 18A was perfectly maintained and the orientation remained interfacial (Fig. 4.3). The binding energy of 18A decreases by 0.3

kcal/mol from χ = 0 to 0.5 (Fig. 4.4). In experiment, it is reported that the binding free energy of 18A decreases by approximately 0.5 kcal/mol as the mole fraction of DOPE in POPC/DOPE vesicles increases from 0 to 0.5 (164).

$^{KK}pL_{15}$

$^{KK}pL_{15}$ is a designed hydrophobic peptide of 21 residues. According to experiment, the peptide is helical and binds membranes at either transmembrane or interfacial orientation (165). Therefore, at the beginning of our simulation the peptide was placed both parallel to the bilayer at the interface and inserted perpendicular to the bilayer.

During the simulations the helical structure of the peptide was maintained, except that the N-terminus of the interfacial orientation occasionally unfolded. From Fig. 4.3 it can be seen that the interfacial orientation lies right at the interface, while the transmembrane orientation spans completely across the hydrophobic core. In Fig. 4.4A the binding energy of interfacial $^{KK}pL_{15}$ increases by 0.3 kcal/mol from χ = 0 to 0.8, while in Fig. 4.4B the effective energy decreases by 0.2 kcal/mol. As explained above, Fig. 4B gives the intrinsic contribution of the lipid composition while Fig. 4.4A includes the effect of changes in peptide configuration or conformation. Note that in Table 4.4 E^{LAT} of interfacial $^{KK}pL_{15}$ decreases with χ, while E^{IMM1} increases. In Fig. 4.4A the binding energy of transmembrane $^{KK}pL_{15}$ increases by 0.8 kcal/mol from χ = 0 to 0.8. This indicates that the transmembrane orientation becomes less stable than the interfacial orientation as DOPE is added. In experiment, the transition between the two orientations of $^{KK}pL_{15}$ was studied with tryptophan fluorescence. A red-shift of the emission was observed as POPE was added to the

POPC vesicles, indicating that non-bilayer lipids stabilize the binding of the interfacial orientation (165). This is in agreement with the present calculations.

4.5 Discussion

In this study we proposed a simple approach for implicit modeling of the lateral pressure across lipid bilayers. The pressure profile was treated as symmetric with respect to the bilayer center and was decomposed within each leaflet into components in the acyl chain and headgroup regions and at the interface. Each component was represented by a Gaussian function. While the parameters for controlling the position and width of the pressure peaks and the magnitude at the interface were estimated by using the data from the previous MD simulations with explicit lipid models, those for the magnitude in the headgroup and acyl chain regions were calculated based on the relation between the lateral pressure and monolayer bending elasticity. This treatment gives better compatibility with the implicit membrane model IMM1 and enables us to easily calculate the pressure profile at various lipid compositions. Based on the model, the interaction energy between the lateral pressure and peptide cross-sectional area consists of two terms: E^{LAT} that arises from the lateral pressure of the pure lipid bilayer, and E^{COM} that arises from the lateral compression of lipids upon peptide binding and is proportional to the peptide/lipid molar ratio.

From Table 4.3 and Table 4.4 it can be seen that in general the incorporation of the lateral pressure into IMM1 gives extra stabilization to the interfacial binding, as a result of the negative pressure at the bilayer interface. For alamethicin, this extra stabilization is about 8 kcal/mol. With this extra term IMM1 predicts the interfacial orientation to be substantially

more stable than the transmembrane one. This seems inconsistent with experiment, in which alamethicin was found to bind lipid bilayers in transmembrane orientation even at very low concentrations (166). This may be due to the fact that IMM1 was parameterized without the lateral pressure term. It contains an adjustable parameter (parameter a in Eq. 10 of Ref. 10), which controls the intensity of electrostatic interaction inside membrane. A decrease in this parameter from 0.85 to 0.80 would lower the binding energy of transmembrane alamethicin by 7 kcal/mol, while causing little change to interfacial alamethicin. Therefore, it is expected that by re-parameterizing the electrostatic interaction, a relative binding energy between the two orientations that is more consistent with experiment could be obtained.

Another important impact of the new term is in the interfacial configuration of alamethicin. While standard IMM1 predicts significant tilt in the interfacial configuration, the lateral pressure term induces a configuration that is parallel to the membrane. A simple test of the validity of the lateral pressure term would be to perform explicit bilayer simulations of interfacial alamethicin starting from both tilted and untilted simulations. If this effect has been captured correctly, both simulations should converge to a parallel orientation.

As DOPE is added, the lateral pressure within the bilayer will change due to the different spontaneous curvature of DOPC and DOPE. From Fig. 4.4 it can be seen that in general DOPE stabilizes interfacial binding and destabilizes transmembrane binding. According to Eq. 4-29 and Eq. 4-31 this change in binding energy is caused by the change in E^{LAT}, and the difference in E^{LAT} between two different mole fractions of DOPE (χ_1 and χ_2) is given by

$$\Delta E^{LAT} = E^{LAT}_{\chi_1} - E^{LAT}_{\chi_2} = h(1-\lambda)\sum_k a_{P,k}\left(p_k^{\chi_1} - p_k^{\chi_2}\right) \tag{4-36}$$

Since transmembrane alamethicin and $^{KK}pL_{15}$ bind in the acyl chain region of the bilayer (Fig. 4.3) where the pressure increases with χ, according to Eq. 4-36 E^{LAT} increases as well. KB1 binds in the headgroup region where the pressure decreases, so E^{LAT} decreases. The average position of melittin and 18A in the simulations is 15.9 Å and 16.1 Å from the bilayer center, which is between the interface and headgroup region, so E^{LAT} also decreases but by a smaller value. The average position of interfacial alamethicin and $^{KK}pL_{15}$ is 15.0 Å and 14.9 Å, so these two peptides have the least E^{LAT} decrease with χ. The difference for interfacial $^{KK}pL_{15}$ in Fig. 4.4A and 4.4B, as mentioned above, is caused by the change in E^{IMM1} as a result of the conformation change with χ.

In this model, possible bilayer expansion upon peptide binding was taken into account through an empirical expansion coefficient λ. Since the true expansion of a bilayer is hard to estimate and depends on the experimental situation, λ was arbitrarily set to 0.5. The value of λ influences the binding energy of peptides (Eq. 4-33). The results obtained with the value 0.5 adopted here happen to be quite close to experiment. For example, experiment gives a binding free energy increase of 0.8 kcal/mol for transmembrane alamethicin from χ = 0 to 0.6, while the value predicted by our model is 0.5 kcal/mol. By further adjusting λ even better agreement with experiment could be achieved.

The model includes significant assumptions. For example, the whole bilayer is divided into slabs and each slab is treated as independent of the others. This assumption would be appropriate if the lipid chain were completely flexible and able to align exactly with the surface of the peptide. However, the bending rigidity of lipids varies with chain unsaturation (105) and content of cholesterol (167), and it is reasonable to expect that this variation can

cause errors in the calculation of E^{LAT} and E^{COM}. Also neglected are the thermodynamic consequences of the lipid rearrangements when a peptide is inserted. These effects have been calculated using mean field theories (168), but they are difficult to incorporate in analytical implicit membrane models.

Another factor that might cause errors is the absence of the bilayer surface deformation in our model. For example, when there is a hydrophobic mismatch between a transmembrane peptide and the bilayer, the surface of the bilayer around the peptide may grow or collapse until the local thickness of the bilayer is equal to the length of the peptide (169). While this deformation avoids the exposure of hydrophobic surfaces to water and grants the binding extra stabilization, it causes frustration to the bilayer curvature (170). To balance these two opposing forces, the peptide may adjust its binding state without causing any changes to the lateral deformation. An example for this is the association of rhodopsin in lipid membranes. While it is not likely to influence the cross-sectional area of the protein, it was proposed that the association could significantly relieve the membrane curvature strain of the monomeric binding state (170).

These concerns notwithstanding, the present model provides an easy and fast way to take into account the effect of membrane lateral pressure in MD simulations and could be applied to larger systems and more complex problems. A potentially interesting application of the model would be to investigate the influence of lipid composition on the conformation and thus the function of membrane proteins. Also it would be interesting if the model can be further improved by incorporating lipid bending rigidity, which would enable the investigation of the influence of lipid unsatuation and cholesterol on peptide/protein binding.

Chapter V

CONCLUSIONS

In summary, from our theoretical studies, we draw the following conclusions:

(1) We extended EEF1 to the MD simulation of metalloproteins. In order to take into consideration of charge transfer between metal ions and ligands, charges at the binding sites of metalloproteins are re-calculated with *ab initio* method. In order to take into consideration of dielectric screening effect at the binding sites, the ligand carboxylates are neutralized differently based on their exposure to solvent water. The MD simulations on calcium-binding proteins show that these modifications give binding structures consistent with experiments. However, the model is limited by that the selection of charges for the carboxylates is arbitrary, and that these charges cannot be modified as the protein structure changes during the simulation. Therefore, in the future we will try to improve our model to remove these limitations.

(2) We extended IMM1 to incorporate the dipole potential for lipid bilayers. The potential curve is generated by fitting into the data from previous explicit MD simulations and is characterized by a high value in the lipid hydrophobic core and a low value in water, joined by a smooth curve around the headgroup region. The model is applied to the MD simulation of the helical peptides alamethicin, WALP23, HAFP, HIVFP, magainin, and p25. The simulations give orientation consistent with experiments and previous explicit MD simulations for all peptides. Also they show that as the membrane dipole potential increases, generally the tilt angle and binding affinity of the peptides increase as well, which is explained by the interaction between the potential and peptide backbone dipole as well as

cationic side chains. It would be interesting that in the future if we could apply this model to the MD simulation of large membrane proteins, and thereby study the conformational change of the proteins caused by the change in membrane dipole potential.

(3) We extended IMM1 to incorporate the lateral pressure for lipid bilayers. The pressure profile is generated by using a combination of three Gaussian functions corresponding to various regions along the lipid chain. The resulting lateral pressure profile features two positive pressure peaks in the acyl chain and headgroup regions, and a negative pressure peak at the interface. The model is used to study the binding of the peptides alamethicin, melittin, KB1, 18A, and $^{KK}pL_{15}$ to the DOPC bilayer. Results show that for alamethicin, a transition from the interfacial to transmembrane orientation is favored as peptide/lipid ratio increases, which is consistent with experiments. Also, simulations of peptides at various DOPE mole fractions indicate that the binding affinity could increase, decrease, or does not change depending on the binding position of the peptides, which have been confirmed by experiments. Future work of this project involves further improving the model by incorporating lipid bending rigidity, which would enable the investigation of the influence of lipid unsatuation and cholesterol on peptide/protein binding.

REFERENCES

1. Alder, B. J., and T. E. Wainwright. 1957. Phase transition for a hard sphere system. *Journal of Chemical Physics* 27:1208-1209.

2. Alder, B. J., and T. E. Wainwright. 1959. Studies in molecular dynamics .1. General method. *Journal of Chemical Physics* 31:459-466.

3. Rahman, A. 1964. Correlations in motion of atoms in liquid argon. *Physical Review a-General Physics* 136:A405-&.

4. Stilling.Fh, and A. Rahman. 1974. Improved simulation of liquid water by molecular-dynamics. *Journal of Chemical Physics* 60:1545-1557.

5. McCammon, J. A., B. R. Gelin, and M. Karplus. 1977. Dynamics of folded proteins. *Nature* 267:585-590.

6. Still, W. C., A. Tempczyk, R. C. Hawley, and T. Hendrickson. 1990. Semianalytical treatment of solvation for molecular mechanics and dynamics. *Journal of the American Chemical Society* 112:6127-6129.

7. Jacopo Tomasi, B. M., Roberto Cammi. 2005. Quantum mechanical continuum solvation models. *Chem. Rev.* 105.

8. Richmond, T. J. 1984. Solvent accessible surface-area and excluded volume in proteins - analytical equations for overlapping spheres and implications for the hydrophobic effect. *Journal of Molecular Biology* 178:63-89.

9. Themis Lazaridis, M. K. 1999. Effective energy function for proteins in solution. *Proteins* 35.

10. Lazaridis, T. 2003. Effective energy function for proteins in lipid membranes.

Proteins 52:176-192.

11. Lazaridis, T. 2005. Implicit solvent simulations of peptide interactions with anionic lipid membranes. *Proteins-Struct. Funct. Bioinform.* 58:518-527.

12. Thomson, A. J., and H. B. Gray. 1998. Bio-inorganic chemistry. *Current Opinion in Chemical Biology* 2:155-158.

13. Waldron, K. J., and N. J. Robinson. 2009. How do bacterial cells ensure that metalloproteins get the correct metal? *Nature Reviews Microbiology* 7:25-35.

14. Natalie C. J. Strynadka, M. N. G. J. 1989. Crystal structures of the helix-loop-helix calcium-binding proteins. *Annu. Rev. Biochem.* 58.

15. David Allouche, J. P., Yves-Henri Sanejouand. 1999. Ca2+/mg2+ exchange in parvalbumin and other ef-hand proteins. A theoretical study. *J. Mol. Biol.* 285.

16. Peter Ahlstrom, O. T., Bo Jonsson. 1988. Molecular dynamics simulation of interfacial water structure and dynamics in a parvalbumin solution. *J. Am. Chem. Soc.* 110.

17. Peter Ahlstrom, O. T., Johan Kordel, Sture Forsen, Bo Jonsson. 1989. A molecular dynamics simulation of bovine calbindin d9k. Molecular structure and dynamics. *Biochemistry* 28.

18. Sylvie Marchand, B. R. 1998. Molecular dynamics study of calbindin d9k in the apo and singly and doubly calcium-loaded states. *Proteins* 33.

19. Christian D. Berweger, W. T., Wilfred F. van Gunsteren. 2000. Molecular-dynamics simulation of the beta domain of metallothionein with a semi-empirical treatment of the metal core. *Proteins* 41.

20. Dimas Suarez, K. M. m., Jr. 2001. Molecular dynamics simulations of the mononuclear zinc-beta-lactamase from bacillus. *J. Am. Chem. Soc.* 123.

21. M. Susan Cates, M. L. T., George N. Phillips. Jr. 2002. Molecular mechanisms of calcium and magnesium binding to parvalbumin. *Biophys. J* 82.

22. Jaroslav Koca, C.-G. Z., Robert C. Rittenhouse, Rich L. Ornstein. 2003. Coordination number of zinc ions in the phosphotriesterase active site by molecular dynamics and quantum mechanics. *J. Compt. Chem.* 24.

23. Feng-Yun Ni, B. C., Zhi-Chun Ding, Fei Zheng, Ming-Jie Zhang, Hou-Ming Wu, Hong-Zhe Sun, Zhong-Xian Huang. 2007. Structural prediction of the beta-domain of metallothionein-3 by molecular dynamics simulation. *Proteins* 68.

24. Martin Lepsik, M. J. F. 2007. Binding of calcium and other metal ions to the ef-hand loops of calmodulin studied by quantum chemical calculations and molecular dynamics simulations. *J. Phys. Chem. B.*

25. Natalia Diaz, D. S. 2007. Molecular dynamics simulations of matrix metalloproteinase 2: Role of the structural metal ions. *Biochemistry*.

26. Lucia Banci, S. S., Peter A. Kollman. 2003. Molecular dynamics simulations of metalloproteins. *Curr. Opin. Chem. Biol.* 7.

27. Lazaridis, T., and M. Karplus. 1999. Effective energy function for proteins in solution. *Proteins* 35:133-152.

28. Spassov, V. Z., L. Yan, and S. Szalma. 2002. Introducing an implicit membrane in generalized born/solvent accessibility continuum solvent models. *J. Phys. Chem. B* 106:8726-8738.

29. Im, W., M. Feig, and C. L. Brooks. 2003. An implicit membrane generalized born theory for the study of structure, stability, and interactions of membrane proteins. *Biophys. J.* 85:2900-2918.

30. Tanizaki, S., and M. Feig. 2005. A generalized born formalism for heterogeneous dielectric environments: Application to the implicit modeling of biological membranes. *J. Chem. Phys.* 122.

31. Marcus, Y. 1985. Ion solvation. *New York: John Wiley & Sons*.

32. M. J. Frisch, G. W. T., H. B. Schlegel, G. E. Scuseria, M. A. Robb, J. R. Cheeseman, V. G. Zakrzewski, J. A. Montgomery Jr., R. E. Stratmann, J. C. Burant, S. Dapprich, J. M. Millam, A. D. Daniels, K. N. Kudin, M. C. Strain, O. Farkas, J. Tomasi, V. Barone, M. Cossi, R. Cammi, B. Mennucci, C. Pomelli, C. Adamo, S. Clifford, J. Ochterski, G. A. Petersson, P. Y. Ayala, Q. Cui, K. Morokuma, P. Salvador, J. J. Dannenberg, D. K. Malick, A. D. Rabuck, K. Raghavachari, J. B. Foresman, J. Cioslowski, J. V. Ortiz, A. G. Baboul, B. B. Stefanov, G. Liu, A. Liashenko, P. Piskorz, I. Komaromi, R. Gomperts, R. L. Martin, D. J. Fox, T. Keith, M. A. Al-Laham, C. Y. Peng, A. Nanayakkara, M. Challacombe, P. M. W. Gill, B. Johnson, W. Chen, M. W. Wong, J. L. Andres, C. Gonzalez, M. Head-Gordon, E. S. Replogle, and J. A. Pople. *Gaussian 98 (Gaussian, Inc., Pittsburgh, PA, 1998).*

33. Brooks, B. R., C. L. Brooks, A. D. Mackerell, L. Nilsson, R. J. Petrella, B. Roux, Y. Won, G. Archontis, C. Bartels, S. Boresch, A. Caflisch, L. Caves, Q. Cui, A. R. Dinner, M. Feig, S. Fischer, J. Gao, M. Hodoscek, W. Im, K. Kuczera, T. Lazaridis, J. Ma, V. Ovchinnikov, E. Paci, R. W. Pastor, C. B. Post, J. Z. Pu, M. Schaefer, B. Tidor, R. M.

Venable, H. L. Woodcock, X. Wu, W. Yang, D. M. York, and M. Karplus. 2009. Charmm: The biomolecular simulation program. *J. Comput. Chem.* 30:1545-1614.

34. Arieh Warshel, P. K. Sharma, Mitsunori Kato, William W. Parson. 2006. Modeling electrostatic effects in proteins. *Biochimica et Biophysica Acta* 1764.

35. Honig, B. H., W. L. Hubbell, and R. F. Flewelling. 1986. Electrostatic interactions in membranes and proteins. *Annu. Rev. Biophys. Biophys. Chem.* 15:163-193.

36. McLaughlin, S. 1989. The electrostatic properties of membranes. *Annu. Rev. Biophys. Biophys. Chem.* 18:113-136.

37. Liberman, E. A., and V. P. Topaly. 1968. Selective transport of ions through bimolecular phospholipid membranes. *Biochim. Biophys. Acta* 163:125-136.

38. Haydon, D. A., and V. B. Myers. 1973. Surface charge, surface dipoles and membrane conductance. *Biochim. Biophys. Acta* 307:429-443.

39. Hladky, S. B., and D. A. Haydon. 1973. Membrane conductance and surface potential. *Biochim. Biophys. Acta* 318:464-468.

40. Clarke, R. J. 2001. The dipole potential of phospholipid membranes and methods for its detection. *Adv. Colloid Interface Sci.* 89:263-281.

41. Gawrisch, K., D. Ruston, J. Zimmerberg, V. A. Parsegian, R. P. Rand, and N. Fuller. 1992. Membrane dipole potentials, hydration forces, and the ordering of water at membrane surfaces. *Biophys. J.* 61:1213-1223.

42. Marrink, S. J., M. Berkowitz, and H. J. C. Berendsen. 1993. Molecular-dynamics simulation of a membrane water interface - the ordering of water and its relation to the hydration force. *Langmuir* 9:3122-3131.

43. Chiu, S. W., M. Clark, V. Balaji, S. Subramaniam, H. L. Scott, and E. Jakobsson. 1995. Incorporation of surface-tension into molecular-dynamics simulation of an interface - a fluid-phase lipid bilayer-membrane. *Biophys. J.* 69:1230-1245.

44. Zhou, F., and K. Schulten. 1995. Molecular-dynamics study of a membrane water interface. *J. Phys. Chem.* 99:2194-2207.

45. Tieleman, D. P., and H. J. C. Berendsen. 1996. Molecular dynamics simulations of a fully hydrated dipalmitoyl phosphatidylcholine bilayer with different macroscopic boundary conditions and parameters. *J. Chem. Phys.* 105:4871-4880.

46. Shinoda, W., M. Shimizu, and S. Okazaki. 1998. Molecular dynamics study on electrostatic properties of a lipid bilayer: Polarization, electrostatic potential, and the effects on structure and dynamics of water near the interface. *J. Phys. Chem. B* 102:6647-6654.

47. Essmann, U., and M. L. Berkowitz. 1999. Dynamical properties of phospholipid bilayers from computer simulation. *Biophys. J.* 76:2081-2089.

48. Berger, O., O. Edholm, and F. Jahnig. 1997. Molecular dynamics simulations of a fluid bilayer of dipalmitoylphosphatidylcholine at full hydration, constant pressure, and constant temperature. *Biophys. J.* 72:2002-2013.

49. Chiu, S. W., E. Jakobsson, S. Subramaniam, and H. L. Scott. 1999. Combined monte carlo and molecular dynamics simulation of fully hydrated dioleyl and palmitoyl-oleyl phosphatidylcholine lipid bilayers. *Biophys. J.* 77:2462-2469.

50. Smondyrev, A. M., and M. L. Berkowitz. 1999. Structure of dipalmitoylphosphatidylcholine/cholesterol bilayer at low and high cholesterol

concentrations: Molecular dynamics simulation. *Biophys. J.* 77:2075-2089.

51. Wilson, M. A., A. Pohorille, and L. R. Pratt. 1989. Study on the liquid vapor interface of water .1. Simulation results of thermodynamic properties and orientational structure - comment. *J. Chem. Phys.* 90:5211-5213.

52. Harder, E., A. D. MacKerell, Jr., and B. Roux. 2009. Many-body polarization effects and the membrane dipole potential. *J. Am. Chem. Soc.* 131:2760-+.

53. Vorobyov, I., and T. W. Allen. 2010. The electrostatics of solvent and membrane interfaces and the role of electronic polarizability. *J. Chem. Phys.* 132:85101-85101.

54. Andersen, O., and M. Fuchs. 1975. Potential-energy barriers to ion-transport within lipid bilayers. *Biophys. J.* 15:795-830.

55. Flewelling, R. F., and W. L. Hubbell. 1986. The membrane dipole potential in a total membrane-potential model - applications to hydrophobic ion interactions with membranes. *Biophys. J.* 49:541-552.

56. Brockman, H. 1994. Dipole potential of lipid-membranes. *Chem. Phys. Lipids* 73:57-79.

57. Gross, E., R. S. Bedlack, and L. M. Loew. 1994. Dual-wavelength ratiometric fluorescence measurement of the membrane dipole potential. *Biophys. J.* 67:208-216.

58. Wang, L. G., P. S. Bose, and F. J. Sigworth. 2006. Using cryo-em to measure the dipole potential of a lipid membrane. *Proc. Natl. Acad. Sci. USA* 103:18528-18533.

59. Pickar, A. D., and R. Benz. 1978. Transport of oppositely charged lipophilic probe ions in lipid bilayer membranes having various structures. *J. Membr. Biol.* 44:353-376.

60. Simon, S. A., and T. J. McIntosh. 1989. Magnitude of the solvation pressure depends on dipole potential. *Proc. Natl. Acad. Sci. USA* 86:9263-9267.

61. McIntosh, T. J., S. A. Simon, D. Needham, and C. H. Huang. 1992. Interbilayer interactions between sphingomyelin and sphingomyelin cholesterol bilayers. *Biochemistry* 31:2020-2024.

62. Lairion, F., and E. A. Disalvo. 2004. Effect of phloretin on the dipole potential of phosphatidylcholine, phosphatidylethanolamine, and phosphatidylglycerol monolayers. *Langmuir* 20:9151-9155.

63. Starke-Peterkovic, T., and R. J. Clarke. 2009. Effect of headgroup on the dipole potential of phospholipid vesicles. *Eur. Biophys. J. Biophy.* 39:103-110.

64. Andersen, O. S., A. Finkelstein, I. Katz, and A. Cass. 1976. Effect of phloretin on permeability of thin lipid-membranes. *J. Gen. Physiol.* 67:749-771.

65. Melnik, E., R. Latorre, J. E. Hall, and D. C. Tosteson. 1977. Phloretin-induced changes in ion-transport across lipid bilayer membranes. *J. Gen. Physiol.* 69:243-257.

66. Reyes, J., F. Greco, R. Motais, and R. Latorre. 1983. Phloretin and phloretin analogs - mode of action in planar lipid bilayers and monolayers. *J. Membr. Biol.* 72:93-103.

67. Franklin, J. C., and D. S. Cafiso. 1993. Internal electrostatic potentials in bilayers - measuring and controlling dipole potentials in lipid vesicles. *Biophys. J.* 65:289-299.

68. Tu, K. C., M. L. Klein, and D. J. Tobias. 1998. Constant-pressure molecular dynamics investigation of cholesterol effects in a dipalmitoylphosphatidylcholine bilayer. *Biophys. J.* 75:2147-2156.

69. Luchian, T., and L. Mereuta. 2006. Phlorizin- and 6-ketocholestanol-mediated

antagonistic modulation of alamethicin activity in phospholipid planar membranes. *Langmuir* 22:8452-8457.

70. Brasseur, R., T. Pillot, L. Lins, J. Vandekerckhove, and M. Rosseneu. 1997. Peptides in membranes: Tipping the balance of membrane stability. *Trends Biochem. Sci* 22:167-171.

71. La Rocca, P., Y. Shai, and M. S. P. Sansom. 1999. Peptide-bilayer interactions: Simulations of dermaseptin b, an antimicrobial peptide. *Biophys. Chem.* 76:145-159.

72. Lin, J. H., N. A. Baker, and J. A. McCammon. 2002. Bridging implicit and explicit solvent approaches for membrane electrostatics. *Biophys. J.* 83:1374-1379.

73. Davis, J. E., O. Raharnan, and S. Patel. 2009. Molecular dynamics simulations of a dmpc bilayer using nonadditive interaction models. *Biophys. J.* 96:385-402.

74. Hogberg, C. J., and A. P. Lyubartsev. 2008. Effect of local anesthetic lidocaine on electrostatic properties of a lipid bilayer. *Biophys. J.* 94:525-531.

75. Patra, M., M. Karttunen, M. T. Hyvonen, E. Falck, P. Lindqvist, and I. Vattulainen. 2003. Molecular dynamics simulations of lipid bilayers: Major artifacts due to truncating electrostatic interactions. *Biophys. J.* 84:3636-3645.

76. Gurtovenko, A. A., M. Patra, M. Karttunen, and I. Vattulainen. 2004. Cationic dmpc/dmtap lipid bilayers: Molecular dynamics study. *Biophys. J.* 86:3461-3472.

77. Mojumdar, E. H., and A. P. Lyubartsev. 2010. Molecular dynamics simulations of local anesthetic articaine in a lipid bilayer. *Biophys. Chem.* 153:27-35.

78. Vorobyov, I., B. Bekker, and T. W. Allen. 2010. Electrostatics of deformable lipid membranes. *Biophys. J.* 98:2904-2913.

79. Tamm, L. K., and I. Bartoldus. 1990. Secondary structure of a mitochondrial signal peptide in lipid bilayer-membranes. *FEBS Lett.* 272:29-33.

80. Bak, M., R. P. Bywater, M. Hohwy, J. K. Thomsen, K. Adelhorst, H. J. Jakobsen, O. W. Sorensen, and N. C. Nielsen. 2001. Conformation of alamethicin in oriented phospholipid bilayers determined by n-15 solid-state nuclear magnetic resonance. *Biophys. J.* 81:1684-1698.

81. Park, S. H., and S. J. Opella. 2005. Tilt angle of a trans-membrane helix is determined by hydrophobic mismatch. *J. Mol. Biol.* 350:310-318.

82. Ozdirekcan, S., C. Etchebest, J. A. Killian, and P. F. J. Fuchs. 2007. On the orientation of a designed transmembrane peptide: Toward the right tilt angle? *J. Am. Chem. Soc.* 129:15174-15181.

83. Ramamoorthy, A., S. K. Kandasamy, D. K. Lee, S. Kidambi, and R. G. Larson. 2007. Structure, topology, and tilt of cell-signaling peptides containing nuclear localization sequences in membrane bilayers determined by solid-state nmr and molecular dynamics simulation studies. *Biochemistry* 46:965-975.

84. Sammalkorpi, M., and T. Lazaridis. 2007. Configuration of influenza hemagglutinin fusion peptide monomers and oligomers in membranes. *BBA-Biomembranes* 1768:30-38.

85. Boughton, A. P., I. Andricioaei, and Z. Chen. 2010. Surface orientation of magainin 2: Molecular dynamics simulation and sum frequency generation vibrational spectroscopic studies. *Langmuir* 26:16031-16036.

86. Castano, S., and B. Desbat. 2005. Structure and orientation study of fusion peptide

fp23 of gp41 from hiv-1 alone or inserted into various lipid membrane models (mono-, bi- and multibi-layers) by ft-ir spectroscopies and brewster angle microscopy. *BBA-Biomembranes* 1715:81-95.

87. Kamath, S., and T. C. Wong. 2002. Membrane structure of the human immunodeficiency virus gp41 fusion domain by molecular dynamics simulation. *Biophys. J.* 83:135-143.

88. Brasseur, R., H. Deloof, J. M. Ruysschaert, and M. Rosseneu. 1988. Conformational-analysis of lipid-associating proteins in a lipid environment. *Biochim. Biophys. Acta* 943:95-102.

89. Goormaghtigh, E., I. Martin, M. Vandenbranden, R. Brasseur, and J. M. Ruysschaert. 1989. Secondary structure and orientation of a chemically synthesized mitochondrial signal sequence in phospholipid-bilayers. *Biochem. Biophys. Res. Commun.* 158:610-616.

90. Voglino, L., T. J. McIntosh, and S. A. Simon. 1998. Modulation of the binding of signal peptides to lipid bilayers by dipoles near the hydrocarbon-water interface. *Biochemistry* 37:12241-12252.

91. Cladera, J., and P. O'Shea. 1998. Intramembrane molecular dipoles affect the membrane insertion and folding of a model amphiphilic peptide. *Biophys. J.* 74:2434-2442.

92. Asawakarn, T., J. Cladera, and P. O'Shea. 2001. Effects of the membrane dipole potential on the interaction of saquinavir with phospholipid membranes and plasma membrane receptors of caco-2 cells. *J. Biol. Chem.* 276:38457-38463.

93. Allende, D., A. Vidal, S. A. Simon, and T. J. McIntosh. 2003. Bilayer interfacial properties modulate the binding of amphipathic peptides. *Chem. Phys. Lipids* 122:65-76.

94. Buzon, V., and J. Cladera. 2006. Effect of cholesterol on the interaction of the hiv gp41 fusion peptide with model membranes. Importance of the membrane dipole potential. *Biochemistry* 45:15768-15775.

95. Wessman, P., A. A. Stromstedt, M. Malmsten, and K. Edwards. 2008. Melittin-lipid bilayer interactions and the role of cholesterol. *Biophys. J.* 95:4324-4336.

96. Marsh, D. 1996. Lateral pressure in membranes. *BBA-Rev. Biomembranes* 1286:183-223.

97. Marsh, D. 2007. Lateral pressure profile, spontaneous curvature frustration, and the incorporation and conformation of proteins in membranes. *Biophys. J.* 93:3884-3899.

98. Helfrich, W. 1981. Amphiphilic mesophases made of defects. North-Holland publishing company, Amsterdam.

99. Engelhardt, H., H. P. Duwe, and E. Sackmann. 1985. Bilayer bending elasticity measured by fourier-analysis of thermally excited surface undulations of flaccid vesicles. *J. Phys. Lett.-Paris* 46:L395-L400.

100. Bivas, I., P. Hanusse, P. Bothorel, J. Lalanne, and O. Aguerrechariol. 1987. An application of the optical microscopy to the determination of the curvature elastic-modulus of biological and model membranes. *J. Phys.-Paris* 48:855-867.

101. Evans, E., and W. Rawicz. 1990. Entropy-driven tension and bending elasticity in condensed-fluid membranes. *Phys. Rev. Lett.* 64:2094-2097.

102. Rand, R. P., N. L. Fuller, S. M. Gruner, and V. A. Parsegian. 1990. Membrane curvature, lipid segregation, and structural transitions for phospholipids under dual-solvent stress. *Biochemistry* 29:76-87.

103. Leikin, S., M. M. Kozlov, N. L. Fuller, and R. P. Rand. 1996. Measured effects of diacylglycerol on structural and elastic properties of phospholipid membranes. *Biophys. J.* 71:2623-2632.

104. Templer, R. H., B. J. Khoo, and J. M. Seddon. 1998. Gaussian curvature modulus of an amphiphilic monolayer. *Langmuir* 14:7427-7434.

105. Rawicz, W., K. C. Olbrich, T. McIntosh, D. Needham, and E. Evans. 2000. Effect of chain length and unsaturation on elasticity of lipid bilayers. *Biophys. J.* 79:328-339.

106. Siegel, D. P., and M. M. Kozlov. 2004. The gaussian curvature elastic modulus of n-monomethylated dioleoylphosphatidylethanolamine: Relevance to membrane fusion and lipid phase behavior. *Biophys. J.* 87:366-374.

107. Gawrisch, K., and L. L. Holte. 1996. Nmr investigations of non-lamellar phase promoters in the lamellar phase state. *Chem. Phys. Lipids* 81:105-116.

108. Templer, R. H., S. J. Castle, A. R. Curran, G. Rumbles, and D. R. Klug. 1998. Sensing isothermal changes in the lateral pressure in model membranes using di-pyrenyl phosphatidylcholine. *Faraday Discuss.* 111:41-53.

109. Szleifer, I., D. Kramer, A. Benshaul, D. Roux, and W. M. Gelbart. 1988. Curvature elasticity of pure and mixed surfactant films. *Phys. Rev. Lett.* 60:1966-1969.

110. Szleifer, I., A. Benshaul, and W. M. Gelbart. 1990. Chain packing statistics and thermodynamics of amphiphile monolayers. *J. Phys. Chem.* 94:5081-5089.

111. Szleifer, I., D. Kramer, A. Benshaul, W. M. Gelbart, and S. A. Safran. 1990. Molecular theory of curvature elasticity in surfactant films. *J. Chem. Phys.* 92:6800-6817.

112. Xiang, T. X., and B. D. Anderson. 1994. Molecular-distributions in interphases - statistical-mechanical theory combined with molecular-dynamics simulation of a model lipid bilayer. *Biophys. J.* 66:561-572.

113. Cantor, R. S. 1997. The lateral pressure profile in membranes: A physical mechanism of general anesthesia. *Biochemistry* 36:2339-2344.

114. Cantor, R. S. 1999. The influence of membrane lateral pressures on simple geometric models of protein conformational equilibria. *Chem. Phys. Lipids* 101:45-56.

115. Cantor, R. S. 1999. Lipid composition and the lateral pressure profile in bilayers. *Biophys. J.* 76:2625-2639.

116. Cantor, R. S. 2002. Size distribution of barrel-stave aggregates of membrane peptides: Influence of the bilayer lateral pressure profile. *Biophys. J.* 82:2520-2525.

117. Lindahl, E., and O. Edholm. 2000. Spatial and energetic-entropic decomposition of surface tension in lipid bilayers from molecular dynamics simulations. *J. Chem. Phys.* 113:3882-3893.

118. Gullingsrud, J., and K. Schulten. 2004. Lipid bilayer pressure profiles and mechanosensitive channel gating. *Biophys. J.* 86:3496-3509.

119. Patra, M. 2005. Lateral pressure profiles in cholesterol-dppc bilayers. *Eur. Biophys. J. Biophy.* 35:79-88.

120. Sonne, J., F. Y. Hansen, and G. H. Peters. 2005. Methodological problems in pressure

profile calculations for lipid bilayers. *J. Chem. Phys.* 122.

121. Carrillo-Tripp, M., and S. E. Feller. 2005. Evidence for a mechanism by which omega-3 polyunsaturated lipids may affect membrane protein function. *Biochemistry* 44:10164-10169.

122. Ollila, O. H. S., T. Rog, M. Karttunen, and I. Vattulainen. 2007. Role of sterol type on lateral pressure profiles of lipid membranes affecting membrane protein functionality: Comparison between cholesterol, desmosterol, 7-dehydrocholesterol and ketosterol. *J. Struct. Biol.* 159:311-323.

123. Ollila, S., M. T. Hyvonen, and I. Vattulainen. 2007. Polyunsaturation in lipid membranes: Dynamic properties and lateral pressure profiles. *J. Phys. Chem. B* 111:3139-3150.

124. Griepernau, B., and R. A. Boeckmann. 2008. The influence of 1-alkanols and external pressure on the lateral pressure profiles of lipid bilayers. *Biophys. J.* 95:5766-5778.

125. Terama, E., O. H. S. Ollila, E. Salonen, A. C. Rowat, C. Trandum, P. Westh, M. Patra, M. Karttunen, and I. Vattulainen. 2008. Influence of ethanol on lipid membranes: From lateral pressure profiles to dynamics and partitioning. *J. Phys. Chem. B* 112:4131-4139.

126. Jerabek, H., G. Pabst, M. Rappolt, and T. Stockner. 2010. Membrane-mediated effect on ion channels induced by the anesthetic drug ketamine. *J. Am. Chem. Soc.* 132:7990-7997.

127. Ollila, O. H. S., H. J. Risselada, M. Louhivuori, E. Lindahl, I. Vattulainen, and S. J. Marrink. 2009. 3d pressure field in lipid membranes and membrane-protein

complexes. *Phys. Rev. Lett.* 102.

128. Baoukina, S., S. J. Marrink, and D. P. Tieleman. 2010. Lateral pressure profiles in lipid monolayers. *Faraday Discuss.* 144:393-409.

129. Venturoli, M., and B. Smit. 1999. Simulating the self-assembly of model membranes. *Physchemcomm* 2.

130. Harries, D., and A. BenShaul. 1997. Conformational chain statistics in a model lipid bilayer: Comparison between mean field and monte carlo calculations. *J. Chem. Phys.* 106:1609-1619.

131. Brink-van der Laan, E. V., J. A. Killian, and B. de Kruijff. 2004. Nonbilayer lipids affect peripheral and integral membrane proteins via changes in the lateral pressure profile. *BBA-Biomembranes* 1666:275-288.

132. Keller, S. L., S. M. Bezrukov, S. M. Gruner, M. W. Tate, I. Vodyanoy, and V. A. Parsegian. 1993. Probability of alamethicin conductance states varies with nonlamellar tendency of bilayer phospholipids. *Biophys. J.* 65:23-27.

133. Lewis, J. R., and D. S. Cafiso. 1999. Correlation between the free energy of a channel-forming voltage-gated peptide and the spontaneous curvature of bilayer lipids. *Biochemistry* 38:5932-5938.

134. van Klompenburg, W., M. Paetzel, J. M. de Jong, R. E. Dalbey, R. A. Demel, G. von Heijne, and B. de Kruijff. 1998. Phosphatidylethanolamine mediates insertion of the catalytic domain of leader peptidase in membranes. *FEBS Lett.* 431:75-79.

135. Botelho, A. V., N. J. Gibson, R. L. Thurmond, Y. Wang, and M. F. Brown. 2002. Conformational energetics of rhodopsin modulated by nonlamellar-forming lipids.

Biochemistry 41:6354-6368.

136. Senisterra, G., and R. M. Epand. 1993. Role of membrane defects in the regulation of the activity of protein-kinase-c. *Arch. Biochem. Biophys.* 300:378-383.

137. Stubbs, C. D., and S. J. Slater. 1996. The effects of non-lamellar forming lipids on membrane protein-lipid interactions. *Chem. Phys. Lipids* 81:185-195.

138. Cornell, R. B., and R. S. Arnold. 1996. Modulation of the activities of enzymes of membrane lipid metabolism by non-bilayer-forming lipids. *Chem. Phys. Lipids* 81:215-227.

139. Attard, G. S., R. H. Templer, W. S. Smith, A. N. Hunt, and S. Jackowski. 2000. Modulation of ctp : Phosphocholine cytidylyltransferase by membrane curvature elastic stress. *Proc. Natl. Acad. Sci. USA* 97:9032-9036.

140. Mottamal, M., and T. Lazaridis. 2006. Voltage-dependent energetics of alamethicin monomers in the membrane. *Biophys. Chem.* 122:50-57.

141. Lazaridis, T. 2005. Structural determinants of transmembrane beta-barrels. *J. Chem. Theory Comput.* 1:716-722.

142. Mihajlovic, M., and T. Lazaridis. 2010. Antimicrobial peptides in toroidal and cylindrical pores. *BBA-Biomembranes* 1798:1485-1493.

143. Mihajlovic, M., and T. Lazaridis. 2010. Antimicrobial peptides bind more strongly to membrane pores. *BBA-Biomembranes* 1798:1494-1502.

144. Zhan, H., and T. Lazaridis. 2012. Influence of the membrane dipole potential on peptide binding to lipid bilayers. *Biophys. Chem.* 161:1-7.

145. Marsh, D. 2006. Elastic curvature constants of lipid monolayers and bilayers. *Chem.*

Phys. Lipids 144:146-159.

146. Marsh, D., A. Watts, and I. C. P. Smith. 1983. Dynamic structure and phase-behavior of "dimyristoylphosphatidylethanolamine bilayers studied by deuterium nuclear magnetic-resonance. *Biochemistry* 22:3023-3026.

147. Perly, B., I. C. P. Smith, and H. C. Jarrell. 1985. Effects of the replacement of a double-bond by a cyclopropane ring in phosphatidylethanolamines - a h-2 nmr-study of phase-transitions and molecular-organization. *Biochemistry* 24:1055-1063.

148. Cullis, P. R., M. J. Hope, and C. P. S. Tilcock. 1986. Lipid polymorphism and the roles of lipids in membranes. *Chem. Phys. Lipids* 40:127-144.

149. Rand, R. P., and V. A. Parsegian. 1989. Hydration forces between phospholipid-bilayers. *Biochim. Biophys. Acta* 988:351-376.

150. Rand, R. P. Structural parameters of aqueous phospholipid mixtures.

151. Cafiso, D. S. 1994. Alamethicin - a peptide model for voltage gating and protein membrane interactions. *Annu. Rev. Biophys. Biomol. Struct.* 23:141-165.

152. Huang, H. W., and Y. Wu. 1991. Lipid-alamethicin interactions influence alamethicin orientation. *Biophys. J.* 60:1079-1087.

153. He, K., S. J. Ludtke, W. T. Heller, and H. W. Huang. 1996. Mechanism of alamethicin insertion into lipid bilayers. *Biophys. J.* 71:2669-2679.

154. Chen, F. Y., M. T. Lee, and H. W. Huang. 2002. Sigmoidal concentration dependence of antimicrobial peptide activities: A case study on alamethicin. *Biophys. J.* 82:908-914.

155. Huang, H. W. 2009. Free energies of molecular bound states in lipid bilayers: Lethal

concentrations of antimicrobial peptides. *Biophys. J.* 96:3263-3272.

156. Chen, F. Y., M. T. Lee, and H. W. Huang. 2003. Evidence for membrane thinning effect as the mechanism for peptide-induced pore formation. *Biophys. J.* 84:3751-3758.

157. Frey, S., and L. K. Tamm. 1991. Orientation of melittin in phospholipid-bilayers - a polarized attenuated total reflection infrared study. *Biophys. J.* 60:922-930.

158. Bradshaw, J. P., C. E. Dempsey, and A. Watts. 1994. A combined x-ray and neutron-diffraction study of selectively deuterated melittin in phospholipid-bilayers - effect of ph. *Mol. Membr. Biol.* 11:79-86.

159. Batenburg, A. M., J. H. Vanesch, and B. Dekruijff. 1988. Melittin-induced changes of the macroscopic structure of phosphatidylethanolamines. *Biochemistry* 27:2324-2331.

160. Kamimori, H., K. Hall, D. J. Craik, and M. I. Aguilar. 2005. Studies on the membrane interactions of the cyclotides kalata b1 and kalata b6 on model membrane systems by surface plasmon resonance. *Anal. Biochem.* 337:149-153.

161. Huang, Y.-H., M. L. Colgrave, N. L. Daly, A. Keleshian, B. Martinac, and D. J. Craik. 2009. The biological activity of the prototypic cyclotide kalata b1 is modulated by the formation of multimeric pores. *J. Biol. Chem.* 284:20699-20707.

162. Shenkarev, Z. O., K. D. Nadezhdin, V. A. Sobol, A. G. Sobol, L. Skjeldal, and A. S. Arseniev. 2006. Conformation and mode of membrane interaction in cyclotides. Spatial structure of kalata b1 bound to a dodecylphosphocoline micelle. *FEBS J.* 273:2658-2672.

163. Henriques, S. T., Y.-H. Huang, K. J. Rosengren, H. G. Franquelim, F. A. Carvalho, A.

Johnson, S. Sonza, G. Tachedjian, M. A. R. B. Castanho, N. L. Daly, and D. J. Craik. 2011. Decoding the membrane activity of the cyclotide kalata b1 the importance of phosphatidylethanolamine phospholipids and lipid organization on hemolytic and anti-hiv activities. *J. Biol. Chem.* 286:24231-24241.

164. Shintou, K., M. Nakano, T. Kamo, Y. Kuroda, and T. Handa. 2007. Interaction of an amphipathic peptide with phosphatidycholine/phosphatidylethanolamine mixed membranes. *Biophys. J.* 93:3900-3906.

165. Shahidullah, K., and E. London. 2008. Effect of lipid composition on the topography of membrane-associated hydrophobic helices: Stabilization of transmembrane topography by anionic lipids. *J. Mol. Biol.* 379:704-718.

166. North, C. L., M. BarrangerMathys, and D. S. Cafiso. 1995. Membrane orientation of the n-terminal segment of alamethicin determined by solid-state n-15 nmr. *Biophys. J.* 69:2392-2397.

167. Song, J. B., and R. E. Waugh. 1993. Bending rigidity of sopc membranes containing cholesterol. *Biophys. J.* 64:1967-1970.

168. Zemel, A., A. Ben-Shaul, and S. May. 2004. Membrane perturbation induced by interfacially adsorbed peptides. *Biophys. J.* 86:3607-3619.

169. Killian, J. A. 1998. Hydrophobic mismatch between proteins and lipids in membranes. *BBA-Rev. Biomembranes* 1376:401-416.

170. Botelho, A. V., T. Huber, T. P. Sakmar, and M. F. Brown. 2006. Curvature and hydrophobic forces drive oligomerization and modulate activity of rhodopsin in membranes. *Biophys. J.* 91:4464-4477.